https://doi.org/10.15407/ufm.19.04.442

PACS numbers: 61.46.-w, 61.48.-c, 68.37.-d, 68.43.-h, 68.65.-k, 81.05.U-, 81.05.Zx, 81.07.-b, 81.16.-c, 81.70.-q, 82.45.Yz, 82.47.Aa, 88.05.Ec, 88.05.Gh, 88.05.Lg, 88.05.Np, 88.30.G-, 88.30.M-, 88.30.R-, 88.40.-j, 88.40.H-, 88.40.J-, 89.30.-g

O.G. GUGLYA [1], V.A. GUSEV [2], and O.A. LYUBCHENKO [3]

[1] National Science Centre 'Kharkiv Institute of Physics and Technology' of the N.A.S. of Ukraine, 1 Akademichna Str., UA-61108 Kharkiv, Ukraine

[2] North-East Scientific Centre of the N.A.S. and M.E.S. of Ukraine, 8 Bahaliy Str., UA-61000 Kharkiv, Ukraine

[3] National Technical University 'Kharkiv Polytechnic Institute', 2 Kyrpychova Str., UA-61002 Kharkiv, Ukraine

FROM NANOMATERIALS AND NANOTECHNOLOGIES TO THE ALTERNATIVE ENERGY

The use of alternative energy sources in various areas of industry and in everyday life is becoming increasingly important. This is due to the depletion of the sources of hydrocarbon raw materials and, at the same time, the use of fossil fuel leads to environmental degradation and environmental pollution. Among the various possible sources of renewable energy, solar and hydrogen energies are considered the most promising. The main obstacle to widespread use and distribution of them is the lack of materials, which can effectively convert the energy of Sun and hydrogen into electricity and heat. The main requirements for such materials are the high-energy capacity, structural stability, and low price. These properties are inherent in nanocrystalline materials and, therefore, many studies of recent decades have been devoted to them. In this review, a special attention is focused on the three types of nanocrystalline objects of greatest interest for power engineering, namely, solar cells, lithium-ion batteries and solid-state hydrogen storage. Their structural features, manufacturing techniques as well as the relationship between structure and energy capacity are considered. The state and prospects of application of nanocrystalline structures in renewable energy are analysed.

Keywords: alternative energy, nanomaterials, solar cells, lithium-ion battery, hydrogen storage.

Introduction

Life on the Earth and its beginning are inconceivable without the energy that it and all living beings receive from the Sun as the main source of primary energy. Due to this energy for millions of years, there

was an accumulation of secondary hydrocarbon energy sources: coal, oil, gas, and wood. These energy resources meet the needs of humankind by 90%. At the same time, the rate of their use catastrophically exceeds the rate of their accumulation in Earth's crust, in particular, this excess for oil reaches 10^5 times. In this regard, the predictions that large problems with fossil energy sources will arise by 2050 appear to be very realistic [1, 2]. In addition, a significant environmental hazard is an increase in CO_2 concentration that results from the combustion (oxidation) of hydrocarbons. Moreover, if in the middle of the 19th century its concentration did not exceed 280 parts per million (ppm), now it is 390 ppm. By the end of the century, while maintaining the pace of consumption of fossil raw materials, the content of CO_2 is expected to be 600–700 ppm [3]. The increase in the CO_2 content in the atmosphere stimulates the emission of greenhouse gases (N_2O and CH_4) from the soil, which together with CO_2 create a greenhouse effect that has a negative impact on the ecology of our planet.

It is the growing demands of humanity in energy and the aggravating environmental problems that stimulate the intensive developing renewable energy sources (wind, Sun, hydrogen) and the tendency to switch to their use instead of non-renewable hydrocarbon fuel. A further, no less important, argument in favour of developing the renewable energy sources is that their potential capabilities are enormous. For example, the energy of sunlight reaching the surface of Earth for 1 hour exceeds the energy consumed by humankind in 1 year [4]. The maximum effective conversion of solar energy into electricity or heat is possible when using materials that convert the light flux into electrical current in the entire range of light wavelengths as currently applied photovoltaic converters use only a small fraction of the light flux.

Hydrogen itself is not a source of energy. Only its reaction with oxygen leads to the generation of electric current and heat. The energy capacity of hydrogen (143 kJ/g) is significantly higher than the similar values for coal, oil, and gas. However, sadly that widespread use of hydrogen in transport, for industrial and domestic purposes, is hampered by the lack of solid structures that could absorb hydrogen in large (>6 wt.%) quantities, and release it at temperatures not higher than 100 °C.

The total carbon dioxide emission by traffic can be reduced not only through replacing hydrocarbon fuel with hydrogen one. At present, electric vehicles are becoming increasingly widespread with lithium-ion batteries as the main source of electricity. These batteries can accumulate two or three times as many charge as traditional batteries used in cars with internal combustion engines. The main advantage of lithium-ion batteries is the possibility of using electrodes made of materials with various capacitive characteristics. It is the creation of materials that provide fast charging of batteries, and their high electrical power

has been the subject of numerous scientific developments recently (see, for instance, the review [5]).

Thus, the main obstacle that does not currently allow limiting the use of hydrocarbon energy sources and switching to alternative energy is the lack of the materials required for this. These materials have to combine high-energy capacity, reasonable cost, and structural stability. Traditional polycrystalline materials do not meet these conditions. The application of nanomaterials and nanotechnologies is exactly the way that can solve the problem of transition from traditional hydrocarbon to alternative energy sources. This review deals with the description of the features of the structure, properties, methods of production, and application of nanomaterials that can be used in the renewable energy.

Structural Features and Properties of Nanomaterials

It is believed that the first to anticipate the discovery and research of nanomaterials was R. Feynman from California Institute of Technology. In the presentation 'There's plenty of room at the bottom' (1965), he demonstrated the ultrafine-dispersed structures revealed by electron-beam lithography [6]. Ten years later, in 1974, N. Taniguchi from Tokyo University of Science first used the term 'nanotechnology' [7]. In 1976, D. E. Carlson and C. R. Wronski [8] proposed a solar cell concept known as the 'solar amorphous cells'. Wide opportunities in the study of materials at the atomic level appeared after the creation of an atomic-force microscope and a scanning tunnel microscope by G. Binnig, H. Rohrer *et al.* [9, 10]. In 1991, S. Iijima [11] obtained and investigated carbon nanotubes, which use entailed dramatic changes in materials science, electronics, biology, medicine, and ecology.

The creation and evolution of high-resolution research equipment have stimulated the development of numerous techniques for obtaining nanomaterials. In the 80 years, the focus has been on various top-down approaches that have been developed for the commercial production of nanomaterials, particularly, powder technology, intense plastic deformation, controlled crystallization from the amorphous phase, film techniques, *etc.* [12]. H. Gleiter and R. Birringer [13, 14] had contributed immensely to the development of these techniques. In the 2000s, bottom-up approaches became increasingly popular. These approaches include the miniaturization of materials components (up to atomic level) with further self-assembly process leading to the formation of nanostructures. During self-assembly, the physical forces operating at the nanoscale are used to combine basic units into larger stable structures [15].

The objects with less than 100 nm size in at least one of three orthogonal directions are considered nanocrystalline objects. Depending on the method of production, the nanomaterials are divided into 4 categories.

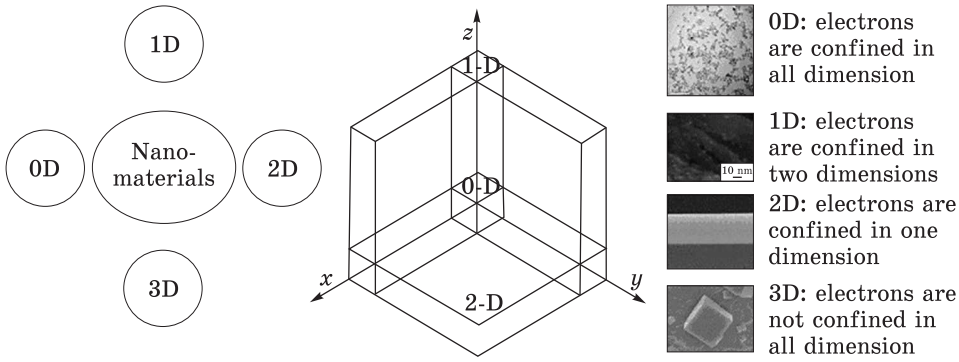

Fig. 1. The classification of nanomaterials based on their confinement [16]

(i) Zero-dimensional nanostructures are limited by nanosize in all three dimensions. Electrons are also localized in all directions. These nanostructures may be amorphous or crystalline, single- or multi-component, exist separately or be embedded in a polycrystalline structure (atomic/molecular clusters).

(ii) One-dimensional nanostructures are limited to nanosize in two dimensions. Electrons are localized in the same directions. Just like the 0-dimensional ones, they may be amorphous or polycrystalline, but their composition must be chemically homogeneous (nanotubes, nanofibers, nanowires, nanorods, and nanofilaments).

(iii) Two-dimensional nanostructures are limited to nanosize in only one direction. They can have different crystal structures and component compositions; they can be embedded into multilayer structures (ultrathin films on a surface and multilayer material, discs, and platelets).

(iv) Three-dimensional nanostructures, nanosize is limited only to the constituent elements. Electrons are not localized. (3*D*-materials contain dispersions of nanoparticles, bundles, nanowires, and nanotubes; see Fig. 1).

Two main features distinguish nanomaterials from bulk structures. The first is that most of the atoms in the nanostructures are related to the surface region (surface effect). The equilibrium vacancy concentration in this region is much higher than the concentration of vacancies inside the bulk materials.

Fig. 2, *a* shows how the proportion of the so-called surface atoms varies with the size of nanoclusters. As a result, the diffusion coefficients in nanomaterials increase considerably (Fig. 2, *b*), and the nanostructures become chemically much more active than the corresponding bulk materials.

The second feature, in addition to the surface effect, a volume dimensional effect is observed in nanomaterials. More precisely, we are talking about the so-called quantum size effect when the electron struc-

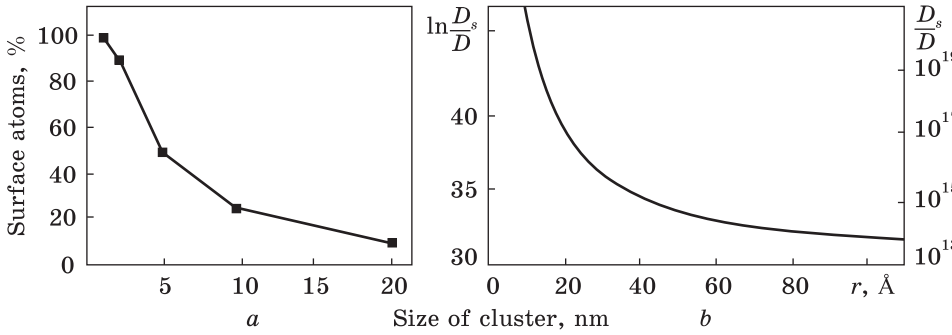

Fig. 2. The percentage of surface atoms in nanoparticles of various diameters (*a*) [17], and the ratio of the surface and bulk diffusion coefficients in the nanoparticle *vs*. its size (*b*) [18]

ture usual for a bulk material is replaced by a series of discrete electronic levels. With the realization of both effects, nanomaterials demonstrate different, in comparison with bulk materials, mechanical, optical, magnetic, electrical, thermal, absorption and other properties. In this review, we consider the outlook for nanostructured materials in lithium-ion batteries, as well as in solar and hydrogen energy.

Nanomaterials for Lithium-Ion Batteries

At present, compared with the 20th century, the needs for rechargeable power sources have increased many times. This is primarily due to the necessity to provide energy for portable electronic devices, aircraft, robotics, medical implants for long periods of time. For these purposes, batteries combining high capacity, low weight, and short recharge times are required. In addition, the need for large-sized rechargeable batteries used in electric vehicles is increasing. Finally, high-capacity batteries are urgently required for wind and solar energy.

In the last decade, the world's battery market has changed from lead acid to Ni–Cd, Cd–Tl, Ni–*M*H (where *M* is a metal), and finally to lithium-ion batteries. Currently, lithium-ion batteries hold leading positions in terms of annual sales, namely, more than $50 billion. First of all, this is due to their high specific electrical capacity and reliability.

The electrodes of the original lithium-ion batteries were made of a powder material with a particle size more than 1 mm, and these batteries had a sufficiently high capacity. In the basic configuration of modern batteries, graphite is used as the negative electrode, and $LiCoO_2$ is the positive one. The use of graphite was the most appropriate decision but was not flawless. The main problem is the low charging rate, which depends on the volume diffusion coefficient of lithium (10^{-8} cm^2sec^{-1}). During charging, the lithium film is growing on the graphite surface,

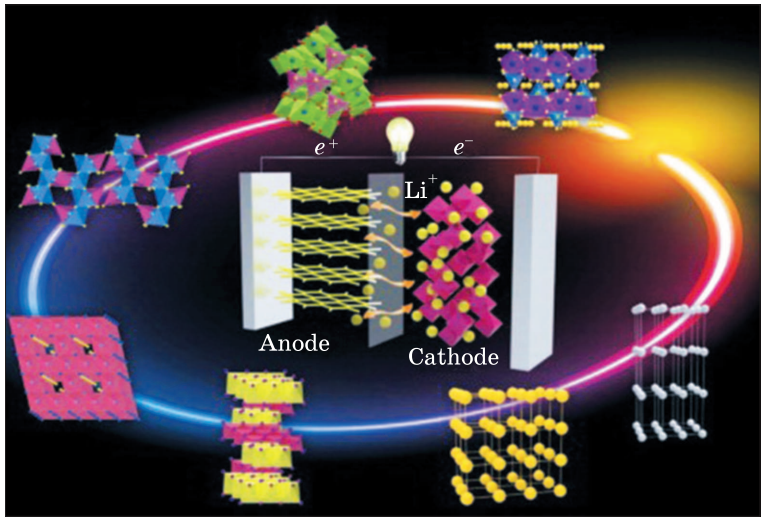

Fig. 3. Schematic representation of a lithium-ion battery and nanostructures used as electrode materials [19]

which leads to short-circuit of the battery. In addition, the graphite–lithium anode has a low gravimetric energy density (340 mAh/kg) as compared to pure lithium (3800 mAh/kg).

This shortfall can be overcome with usage of the nanocrystalline structures instead of the microcrystalline ones since, as it was mention above, just the nanostructures can provide much higher mobility of charge carriers (Fig. 3).

Table 1 summarizes the names of materials prepared by powder technology that are used in lithium-ion batteries. Unfortunately, their use did not give a noticeable improvement in the kinetic properties of the batteries.

Table 1. **Materials used for the electrode production in lithium-ion batteries [20]. Here, metal *M* = Mn, Al, Cr (*a*); *M* = Ni, Cu, Cr (*b*); *M* = Cu, Ni, Fe (*c*); *M* = Fe, Co, Ni Cr, Mn, Cu, Sn (*d*)**

Types	Positive electrodes	Negative electrodes
High energy	$LiNi_xCo_yM_{1-x-y}O_2$ (layered) (*a*) $LiMn_{2-x}M_xO_4$ (spinel) (*b*) MF_x (*c*)	Si, Sn, Sb MO_x (*d*) Graphite
High power	$LiMn_{2-x}Al_xO_{4+\delta}$ (spinel) $LiNi_xCo_{1-2x}Mn_xO_2$ $LiFePO_4$ (olivine)	Hard carbon Graphite $Li_4Ti_5O_{12}$
Long cycle life	$LiFePO_4$ (olivine) $LiMn_{2-x}Al_xO_{4+\delta}$	$Li_4Ti_5O_{12}$ Graphite

Table 2. **Design diffusion times depending on the structure of the material and its diffusion coefficient. Unacceptable times are indicated in italics. (Table contains results calculated according to formula (1))**

D, $cm^2 \cdot s^{-1}$	L, μm				
	0.01	0.1	1.0	10	100
10^{-8}	10^{-4}	10^{-2}	1	10^{2}	10^{4}
10^{-11}	10^{-1}	10	10^{3}	10^{5}	10^{7}
10^{-14}	10^{2}	10^{4}	10^{6}	10^{8}	10^{10}

For substantial improvement of the properties of electrodes in lithium-ion batteries, it is necessary to solve the following problems: increase the free path of lithium in electrode materials, ensure their high electrical conductivity and create the maximum possible number of traps in them. In this case, the configuration of the traps should be such that their filling with lithium does not lead to the destruction of the electrode.

The time during which lithium fills the entire volume of the electrode τ depends on the diffusion coefficient D and on the diffusion length L, that is, on the crystal size, as follows:

$$\tau = L^2/(2D). \quad (1)$$

The diffusion coefficient can be increased by doping the base material with impurities. However, it is difficult to achieve a significant effect in this way. A greater effect can be achieved by transforming the polycrystalline material into a nanocrystalline material (Table 2). Using nanostructured materials with a low diffusion coefficient, lithium saturation with acceptable charging times can be achieved.

The Negative Electrode

There are two ways to get rid of the graphite drawbacks. The first method consists in using nanocrystalline modifications of carbon, *viz.*, fullerenes or carbon nanotubes [21, 22] instead of graphite. In the second case, the structures based on oxides of titanium, iron, manganese, cobalt, and nickel are developed and studied instead of carbon materials. It has been found that the absorption capacity of nanotubes is almost twice as high as that of graphite. However, unfortunately, the surface of nanocarbon structures is subject to blocking by lithium atoms like a graphite surface. The number of publications on the study of the absorption of lithium by oxides is very large [23–26]; therefore, it is impossible to analyse all of them in this short review. Let us dwell on the most promising and studied material, namely, titanium oxide.

Titanium oxide TiO_2 has many advantages: a high insertion potential Li^+/Li (1.5–1.8 V), good specific current capacity, low self-discharge,

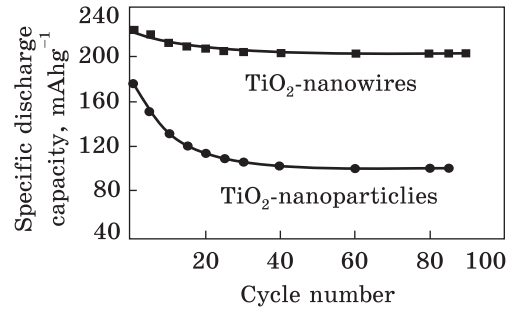

Fig. 4. Specific charge capacity of TiO_2 nanowires and nanoparticles *vs.* the number of charge/discharge cycles [28]

chemical stability, and low cost. In addition, TiO_2 increases its volume after lithium absorption only by 4%, while the graphite increases it by 10%. Disadvantages of TiO_2 are high electrical resistance, the low diffusion coefficient of lithium (10^{-15}–10^{-9} $cm^2 \cdot s^{-1}$), and unsatisfactory theoretical specific capacitance (168–335 mAh/g). Improving the structure and properties of the TiO_2 electrode may be achieved by the creation of one-dimensional nanocrystalline materials: nanorods, nanofibers, nanotubes and core-shell nanowires, the construction of a porous three-dimensional nanostructure, the combination of nanoscale particles with carbon-containing framework structures, and the combination of TiO_2 nanoparticles with other metal oxides.

A comparative study of the specific capacitance of TiO_2 structures in the form of nanowires and equiaxial nanoparticles was carried out in [27, 28]. The diameter of nanowires was the same as the size of nanoparticles (20–40 nm), and the length of the wires was 0.1–1 mm. The small wire diameter facilitates the lithium diffusion along directions orthogonal to their axis. A similar situation has been found in nanoparticles. However, the specific capacitance of nanowires was significantly higher than that of nanoparticles (Fig. 4). According to the authors, nanowires need only a few contact points to ensure the lithium diffusion in the volume of the electrode. In the ensemble of equiaxial nanoparticles, the contact between particles can be disturbed due to a change in their size during the charge/discharge of the battery. As a result, lithium diffusion can be significantly hampered and the battery capacity is reduced. This effect is less significant for finely crystalline structures.

The decrease in the average size of the particle from which the electrode is formed leads to an increase in the area of the specific active

Table 3. **Structural and electrical properties of TiO_2 samples [29]**

	Specific surface area, $m^2 \cdot g^{-1}$	Specific pore volume, $cm^3 \cdot g^{-1}$	Average grain diameter, nm	Average pore diameter, nm	Specific discharge capacity, $mAh \cdot g^{-1}$
Porous-free F-TiO_2	309		5		238
Nanoporous CF-TiO_2	151	0.511	8	7.2	213
Particles	20		20		170

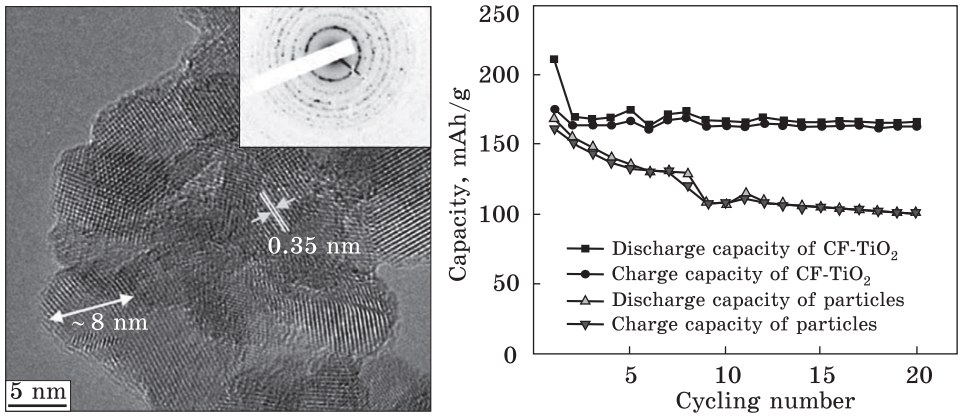

Fig. 5. HR-TEM images of CF-TiO_2 samples with a SAED pattern as inset (*a*), and the variation of specific discharge capacity with respect to the cycle number of CF-TiO_2 and particles (*b*) [29]

absorbing surface. In Ref. [29], nanocrystalline TiO_2 with a grain size of 50 nm was taken as the base material. Two types of nanostructures were additionally obtained by complex chemical-thermal treatment: porous-free F–TiO_2 with 5 nm flake grains, and nanoporous CF–TiO_2 (8 nm flake size, 7.2 nm pore size). It was found that a decrease in grain size not only increases the specific surface area of grains but also enhances the specific capacitance of the electrodes (Table 3).

In addition, the presence of nanopores increases the rate of charge and cyclic stability. Figure 5 shows the high-resolution transmission electron microscopic (HR TEM) image of the CF–TiO_2 structure with its selected area electron diffraction (SAED) pattern and a comparative change in the absorption capacity of CF–TiO_2 and equiaxial nanoparticles.

Further increase in the capacitance and lithium conductivity of materials for negative electrodes is related to the complication both of the component composition and of the pore structure. The strategy for development and use of hybrid structures that combine TiO_2 with transition metal oxides is discussed in [30–32], and interesting results were obtained in [33]. Comparative studies had been carried out concerning the effects of porosity, impurities and carbon coating on the structure, electrical properties and absorption capacity of TiO_2. In the initial state, the material consisted of porous microspheres of diameter ≅1 μm. The porous structure of microspheres was formed due to nanoflakes (Fig. 6, *a*).

Further impregnation of TiO_2 with a solution of $FeCl_3$ and ammonia followed by annealing in air at 500 °C for 1 hour was carried out. As a result, the size of the microspheres remained the same but a large number of thin nanoprecipitations of TiO_2/Fe_2O_3 appeared inside the

nanoflakes (Fig. 6, *b*). Finally, $TiO_2/FeTiO_3$@C carbon-coated films of 2–5 nm thickness were prepared by carbon deposition on TiO_2 and TiO_2/Fe_2O_3 samples. Thus, a transformation of the structure took place, during which the pore size distribution and the specific surface area of the pores changed (Fig. 6c). In the original TiO_2 sample, a non-uniform pore size distribution was observed in the range from 1–2 nm to 200 nm with a pronounced maximum at 10 nm. In $TiO_2/FeTiO_3$@C samples, the maximum shifts to 30 nm, and a many large (up to 250 nm) pores were observed. The specific surface area of the pores was 58.4 m^2/g in the initial samples, and it decreased to 35.1 m^2/g in the samples with a carbon film.

The dependence of the specific capacity of TiO_2-based electrodes on the charge/discharge cycle number is shown in Fig. 7. It can be seen that $TiO_2/FeTiO_3$@C samples have the highest capacity. Already after 100 cycles, their capacity reaches 336 mAh/g. Theoretical evaluation performed by the authors showed that the maximum capacity of $TiO_2/FeTiO_3$@C must not exceed 385 mAh/g. However, a capacity of 441 mAh/g was achieved after 300 charge/discharge cycles.

In the authors' view, the obtained value of specific capacity is a consequence of the synergistic effect in $FeTiO_3$@C structures. For the same reason, the Coulomb efficiency of the $FeTiO_3$@C electrode reaches a value close to 100% after merely 5 charge/discharge cycles.

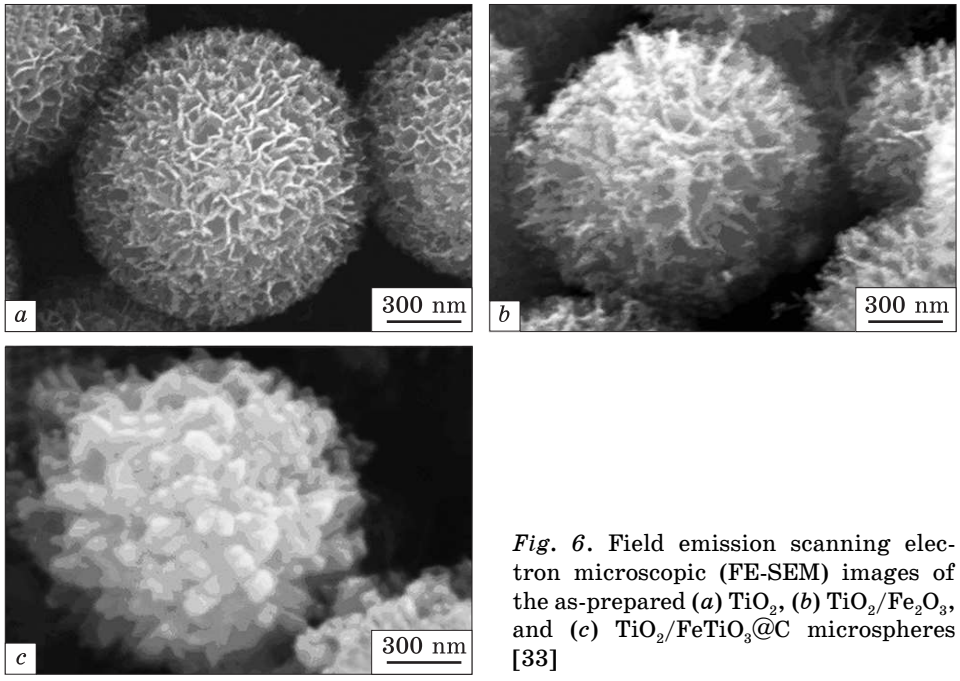

Fig. 6. Field emission scanning electron microscopic (FE-SEM) images of the as-prepared (*a*) TiO_2, (*b*) TiO_2/Fe_2O_3, and (*c*) $TiO_2/FeTiO_3$@C microspheres [33]

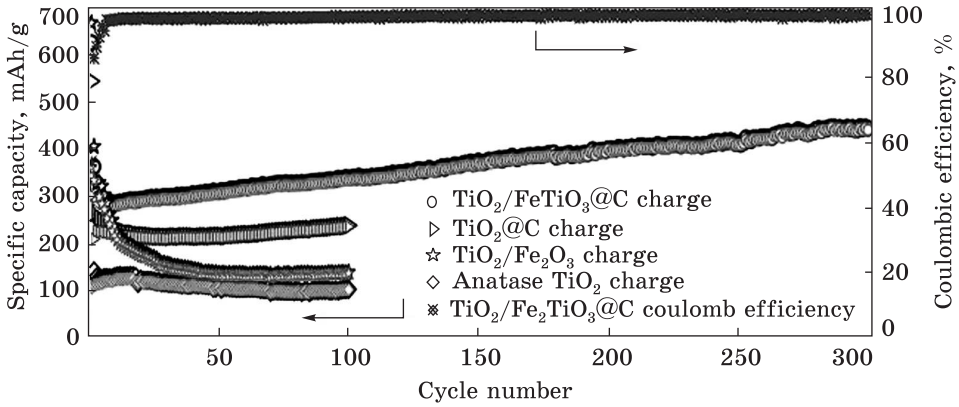

Fig. 7. Cycling performances of TiO_2, TiO_2/Fe_2O_3, TiO_2@C, $TiO_2/FeTiO_3$@C and coulomb efficiency of $TiO_2/FeTiO_3$@C at the current density of 100 $mAhg^{-1}$ [33]

One conclusion compiled from [27–32] shows that the real way to increase the specific absorption capacity and electrical conductivity of TiO_2-based electrodes is nanostructuring the material (nanofibres and nanowires), creating nanopores system (nanoflakes), hybridization of the material by adding oxides based on transition metals, as well as stabilizing their surface activity.

The Positive Electrode

As noted above (Table 1), oxides based on lithium alloys with Fe, Co, Ni Cr, Mn, Cu, Sn are widely used for the production of positive electrodes of lithium-ion batteries including those with a nanocrystalline structure. An essential disadvantage of these materials is their increased chemical activity at the electrode–electrolyte interface, which results in the degradation of the properties of the electrolyte.

The $LiFePO_4$ compound has certain advantages over the above materials: high thermal and chemical stability, and low cost. But most of all, the $LiFePO_4$ structure has the low value of the charge voltage Li^+/Li, namely, 3.4 V. Therefore, this material has less chemical activity in relation to the electrolyte.

In general, charge/discharge processes in the lithium-ion battery include a two-phase reaction between $FePO_4$ and $LiFePO_4$ (Fig. 8). When charging the battery, lithium is removed and $FePO_4$ layer is forming on its surface. During discharging, to the contrary, a surface $LiFePO_4$ layer is forming. Such simultaneous existence of two phases in an electrode is characteristic for polycrystalline structures in which the charge/discharge process is determined by the diffusion of lithium in a solid.

When switching to nanocrystalline structures, the coefficient of lithium diffusion increases substantially and the charging times of the

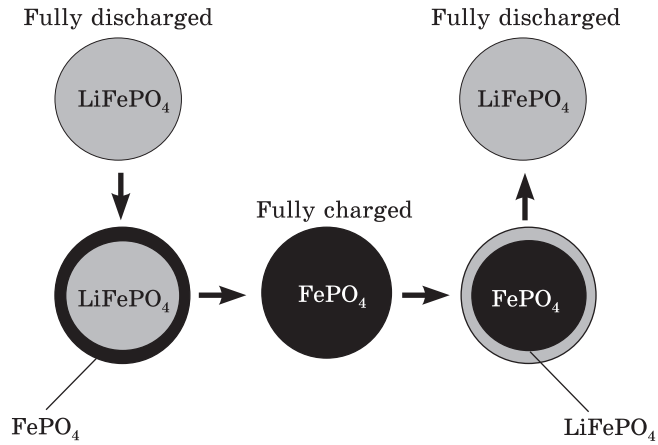

Fig. 8. Schematic representation of the processes during charge/discharge of $LiFePO_4$ [34]

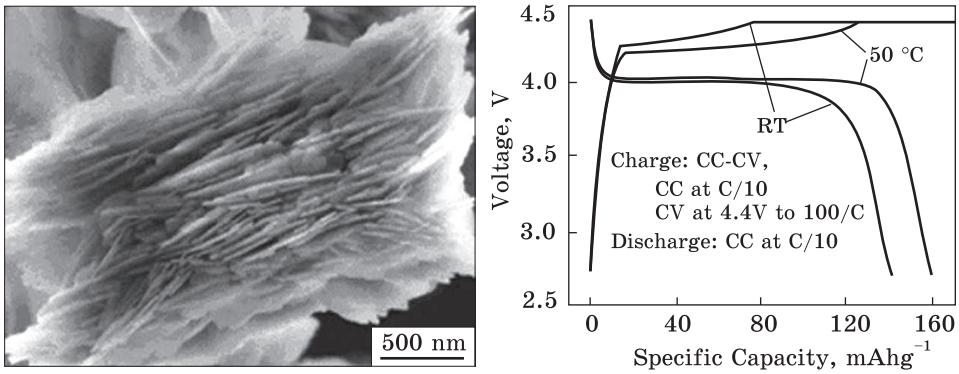

a *b*

Fig. 9. SEM image (*a*), and charge/discharge curves of 2*D* $LiMnPO_4$ (*b*) [36]

battery decrease. In Ref. [35], the kinetic characteristics of the $LiFePO_4$ electrode with grain size was less than 100 nm were studied. Drawing on the results a domino-cascade model of lithium diffusion in such structures was proposed. X-ray diffraction and electron microscopic studies show that deintercalation (intercalation) proceeds through a two-phase reaction between compositions that are very close to $LiFePO_4$ and $FePO_4$, *viz.*, the phases enriched or depleted in lithium (Li-rich $Li_{1-y}FePO_4$ or Li-poor Li_xFePO_4). The authors explain the observed mechanism of the reaction by the existence of structural constraints occurring just at the reaction interface: the minimization of the elastic energy enhances the deintercalation (intercalation) process that occurs as a wave moving through the entire crystal. The stress fields at the boundary between $LiFePO_4$ and $FePO_4$ phases are substantially reduced in the nanocrystalline structures during charge/discharge. As a result, lithium penetrates into the bulk of the lithium grain and the entire thickness of the electrode.

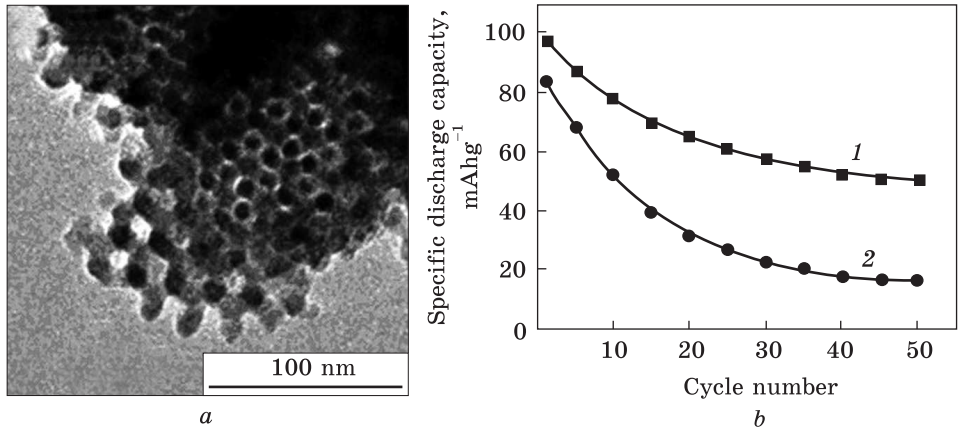

Fig. 10. TEM image of mesoporous LT-$LiCoO_2$ (*a*) and charge storage of lithium as a function of cycle number for mesoporous LT-$LiCoO_2$ and nanoparticle LT-$LiCoO_2$ (*b*) [39]

It is known that in lithium orthorhombic $LiFe(Mn)PO_4$ structures, lithium diffusion is easiest along the '*b*' axis [010] and the diffusion coefficient is about 10^{-8} $cm^2 \cdot s^{-1}$ [36]. This explains the researchers' strategy to create nanoscale structures that would have the smallest size in this direction: 0-dimensional spherical nanoparticles, 1-dimensional rods with the axis oriented along '*a*' or '*c*' directions, 2-dimensional flat formations with a basal plane orthogonal to the axis '*b*'. Fig. 9, *a* shows the structure of $LiMnPO_4$ two-dimensional polyol synthesis structures [37]. This material demonstrates high values of the charge voltage over a wide range of specific capacitance (Fig. 9, *b*).

Ordered nanoporous structures can also be used as a positive electrode material [38, 39]. These materials are formed from micrometer-size particles that contain 2–50 nm pores. Pores have typically the same size and are separated by the walls of 2–8 nm thick. Particles of micrometer size easily compacted into the finished products. The electrical contact is provided due to the close fitting of the walls of the particles to each other. Nanoporous spaces are filled with electrolyte. Thin walls between the pores provide high mobility of lithium ions.

Fig. 10, *a* shows the transmission electron microscopic (TEM) image of the structure of a low-temperature LT-$LiCoO_2$ electrode material [39]. The pores have a size of 4 nm, and the thickness of the walls between the pores is of 7 nm. A comparative study of the cyclic stability of the $LiCoO_2$ structure and material consisting of nanoparticles revealed that the specific surface area of nanoporous objects is 70 m^2/g and of nanoparticle samples is 40 m^2/g. In addition, the nanoporous structures exhibit higher cyclic stability.

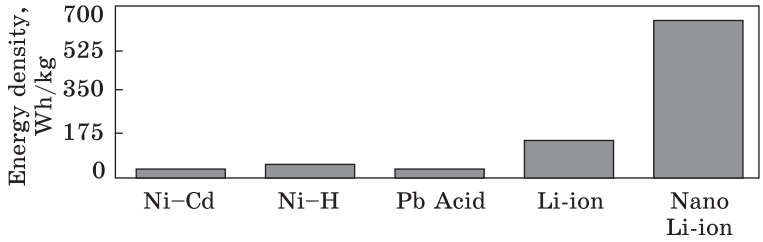

Fig. 11. Energy benefits of using nanomaterials for lithium-ion batteries [40]

Summarizing the data of various researchers, it can be concluded that the use of nanocrystalline, including nanoporous, structures makes it possible to improve significantly the kinetic and absorption properties of both negative and positive electrodes of a lithium-ion battery, and to assess the prospects that nanomaterials science reveals in the development of materials for rechargeable batteries. The opportunities and prospects that nanomaterials open for the creation of rechargeable batteries can be assessed using the comparative results shown in Fig. 11. A more in-depth analysis of the problems faced by researchers in the development and implementation of nanomaterials for lithium-ion batteries is presented in the reviews [5, 19].

Nanomaterials and Solar Energy

It is known that approximately 0.1% of the energy that Earth receives from the Sun is enough for the comfortable existence of humankind. The solar radiation density is 1366 W/m^2. However, not all solar radiation reaches Earth's surface and can be used. Most of the solar energy is lost irrevocably, and only 33% of it can be used (Fig. 12). Nevertheless, humankind would have had enough of this quantity to satisfy its needs in full.

More than 100 years ago, the principle of generating an electric current by semiconductors when they absorbed sunlight (photoelectric effect) was discovered. However, up to the present time, no materials are created that are capable of effectively converting the entire range of wavelengths that reach the surface of Earth into electricity or heat.

In nature, converting solar energy into fossil sources has been going for millions of years. Every moment due to solar radiation there is an accumulation of hydrocarbons in plants, which, in the end, the person converts into heat or electricity. The accumulation of hydrocarbons occurs at the nanocellular level. It is logical to assume that with the help of artificially created nanocrystalline structures, it is possible to achieve a direct conversion of the solar energy into electrical energy with high efficiency, thus excluding the intermediate process of accumulation of hydrocarbon raw materials and its use.

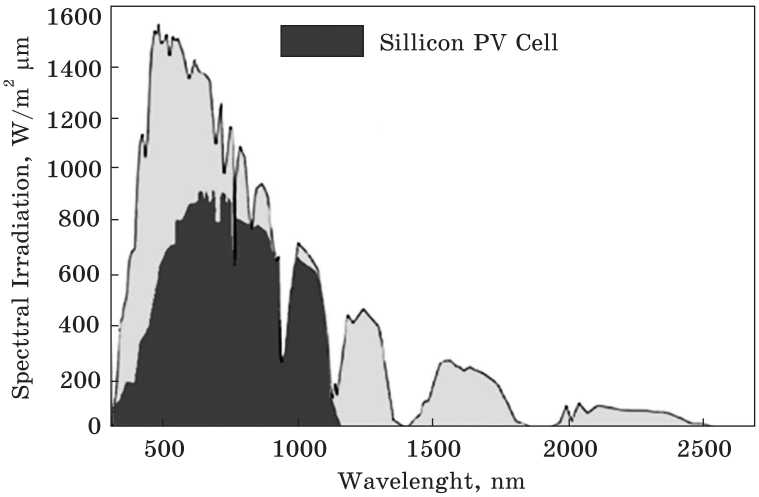

Fig. 12. Earth's energy balance [41]

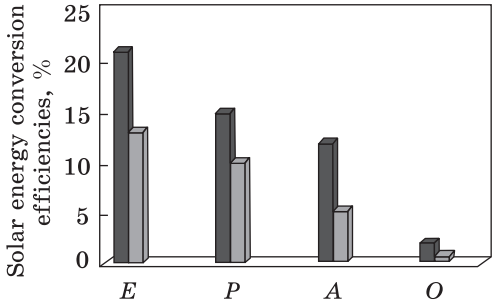

Fig. 13. Power conversion efficiencies of solar cells: single crystalline silicon (*E*), polycrystalline silicon (*P*), amorphous silicon (*A*), organic solar cell (*O*). In each case, both the laboratory (left) and commercial status (right) are shown [42]

Nowadays, there are two types of photovoltaic cells based on silicon (PV cells): crystalline and thin-film cells in the consumer market. Silicon (and also CdTe, CdSe, ZnO, *etc*.) perform two functions simultaneously: they generate a flux of electrons and ensure their movement inside the solar cell. The band gap of crystalline silicon is 1.1 eV, that is, only light quanta with energy equal to or greater than 1.1 eV (wavelength below 1200 nm; Fig. 12) can be used by silicon converters. The efficiency of silicon industrial batteries does not exceed 25% (Fig. 13). Such a low efficiency of solar cells is due to physical limitations, which are superimposed on the process of electron generation and their motion in large-crystal structures. Unfortunately, in these structures, it is very difficult to achieve the simultaneous increase in the optical absorption coefficient (the number of charged particles) and the magnitude of the electron current. In addition, there are losses associated with the design of solar cells.

To improve the photon absorption and photo-carrier collection of silicon solar cells, three-dimensional nanostructures (nanowires [43],

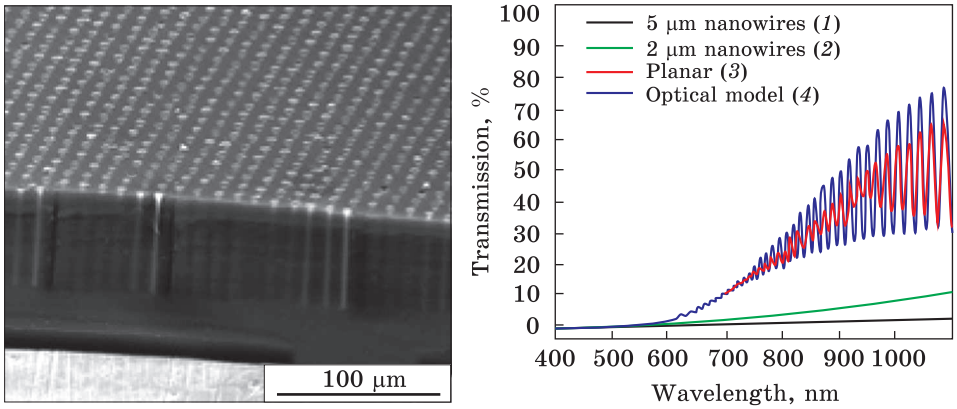

a *b*

Fig. 14. SEM image of the ordered silicon nanowires (*a*). Transmission spectra of thin silicon structures before (*3*, *4*) and after etching to form 2 μm (*2*) and 5 μm (*1*) nanowires (*b*) [43]

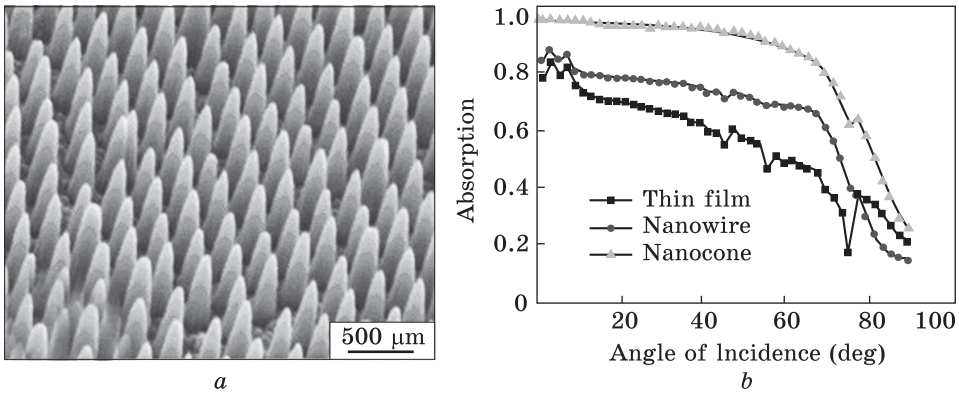

a *b*

Fig. 15. SEM image of Si nanocone arrays (*a*) and angular dependence of light absorption by silicon substrates of various configurations (*b*) [44]

nanopillars, nanocones [44], *etc*.) are being developed. In fact, there is a copying and ordering at the nanolevel of the branched structure of trees that effectively absorb light quanta for their growth. Both top-down and bottom-up methods are used.

For example, Garnett and Yang [43], using selective ion etching technology, fabricated well-ordered arrays of silicon nanowires of 8 μm silicon films (Fig. 14, *a*). Studies of the absorption characteristics of such structures have shown that they increase the path length of incident solar radiation by up to a factor of 73. (Fig. 14, *b*), and the efficiency of solar cells made based on nanowires is above 5%.

The absorption capacity of solar cells can be increased if a nanowire structure is created by the Bottom-up method [43]. Authors obtained

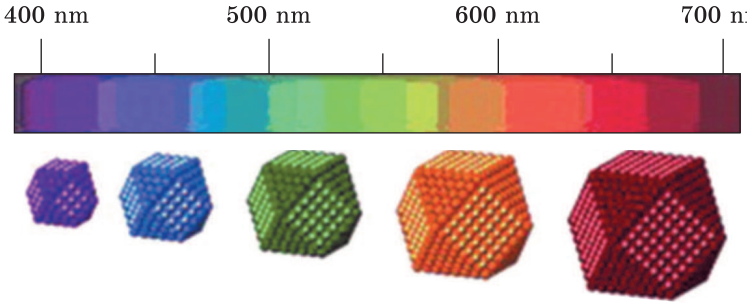

Fig. 16. Dependence of the particle size and colour [45]

material consisting of silicon nanowire arrays. Those arrays having less than 5% areal fraction of wires can achieve up to 96% peak absorption of the solar flux. It is important that the electron current was generated even by solar radiation with a wavelength greater than 1.2 μm.

Absorption properties of solar cells based on silicon can be improved by creating a system of nanocones on their surfaces [44]. A significant improvement in the absorbing properties of cone structure was found even in comparison with nanowire one. The scanning electron microscopy (SEM) image (Fig. 15, *a*) revealed the Si nanocones array. The length of each cone is ≅600 nm; the diameters at the base and at the apex are 300 and 20 nm, respectively. This nanocone structure absorbs up to 90% of sunlight (Fig. 15, *b*) even when the substrate plane is tilted up to an angle of 60° that is essential for its practical application.

Thus, the transition to nanocrystalline silicon made it possible to reduce substantially the fraction of photons reflected from the surface of the solar cell. As a result, the amount of absorbed solar energy increased. In addition, the kinetic properties of charge carriers in the structures consisting of nanowires and nanocones have improved. Nevertheless, the main task to absorb sunlight in the wavelength range from infrared to ultraviolet remained unresolved. The limited possibilities of nanocrystalline silicon are also related to the fact that it generates the charges and acts as their conductor simultaneously.

To improve the solar cells, it was proposed to use inorganic semiconductor structures (TiO_2, ZnO, Nb_2O_5, *etc.*) instead of silicon. These materials are easy to manufacture and inexpensive. The most widespread among the listed semiconductors is titanium oxide TiO_2. In addition to being cheap, this material has good chemical and optical stability, is non-toxic and resistant to corrosion. However, the main advantage of TiO_2 is a possibility of creating the nanostructures with different architectures: nanotubes, nanorods, nanofibres, nanosheets. Such structures have not only a large active surface area but also provide a high mobility of electrons.

Unlike silicon, the main modifications of titanium oxide, anatase and rutile, have a high value of the band gap 3.2 eV and 3 eV, respectively. This means that TiO_2 can generate charge carriers only in the wavelength range of 400 nm or less (ultraviolet region). However, this restriction applies to large-crystal structures. In nanocrystalline semiconductors, the band gap depends on the crystal size d as follows

$$E_g = \hbar/(2md^2), \qquad (2)$$

where $\hbar$ is Plank's constant, and m is the mass of electron.

In accordance with this expression, materials consisting of nanoparticles of different sizes will absorb light of different wavelengths (Fig. 16).

Grätzel *et al.* [46] obtained and investigated two-layer TiO_2 films with a grain size of 20 nm (absorbing centres) and 200–400 nm (scattering centres). It was revealed that such structures can absorb light in the visible range of waves. TiO_2 structures containing nanoparticles and nanorods of varied size in a multilayer configuration for dye-sensitized solar cells were studied in [47]. It was noted that such bilayer system with additional layers of nanorods of well-controlled size inserted between the transparent and the scattering layers (Fig. 17) not only expands the range of absorbed wavelengths but also improves the electrical conductivity of the material.

There is another approach to increase the absorption capacity of TiO_2 structures. To absorb the light in a wide range of wavelengths,

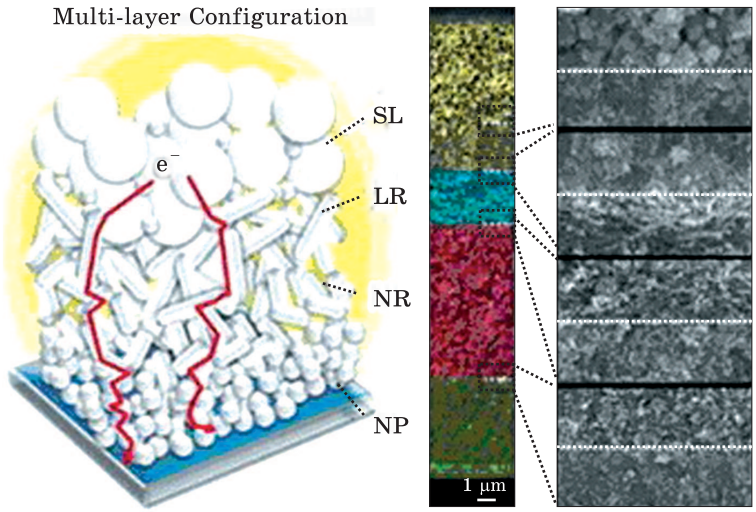

Fig. 17. Schematic demonstration of the structural design for the TiO_2 multilayer film. NP, SL, NR, and LR refer to nanoparticles, scattering layer and TiO_2 nanorods of ≅150 nm and ≅500 nm, respectively [47]

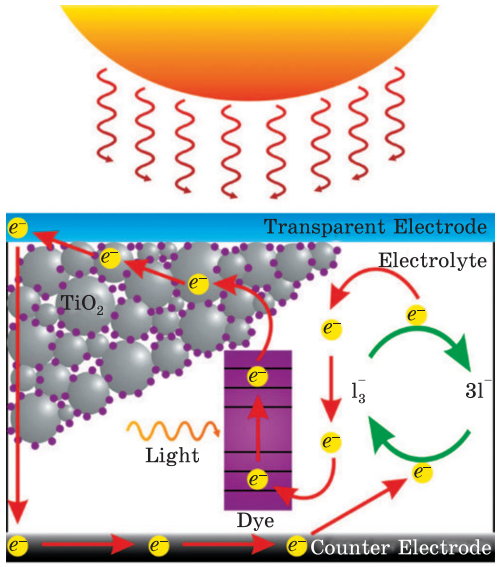

Fig. 18. Schematic structure of dye-sensitized solar cell [48]

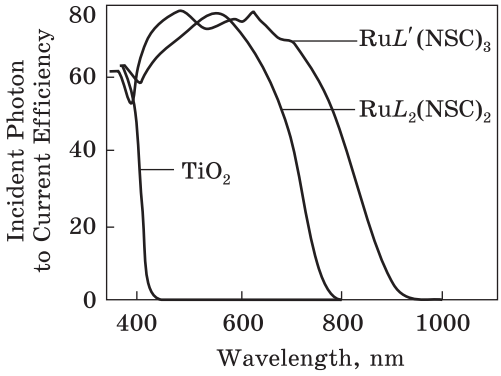

Fig. 19. Photocurrent action spectra obtained with the N_3 (ligand L_2) and the 'black dye' (ligand L') as a sensitizer. The photocurrent response of a bare TiO_2 films is shown for comparison [49]

solar cells based on titanium oxide should contain in their structure the particles with band gap much less than 3 eV. Two types of such structures (dye-sensitized and quantum dots) are currently being investigated. Dye-sensitized solar cells are a mesoporous TiO_2 structure (electrolyte) decorated with molecular clusters consisting of 10–100 molecules (Fig. 18). The material of these molecular clusters is complex chemical compounds based on ruthenium or osmium. Such (dye-sensitized) solar cells do not require vacuum conditions during manufacture; they are plastic and inexpensive. The efficiency of conversion of sunlight reaches 10–12%.

Unlike silicon solar cells, in solar cells with colour centres, titanium oxide serves as a conductor of charged particles, and molecular clusters are converters of light quanta. In 1993 and 2001, a group of scientists developed two types of the ruthenium-based centres: N_3 and 'black dye' [49, 50]. In Ref. [49], it was investigated how the structure of the colour centres and their composition affect the magnitude of the photocurrent (Fig. 19). It is seen that both types of nanosized colour centres significantly extend the range of wavelengths absorbed by the TiO_2 structure. The photocurrent is generated by light photons even from the infrared region. At the same time, the efficiency of conversion of the light flux into energy was achieved by 10.5%.

Finally, there is a third option to increase the sensitivity of solar cells based on TiO_2, namely, to use instead of colour centres the larger

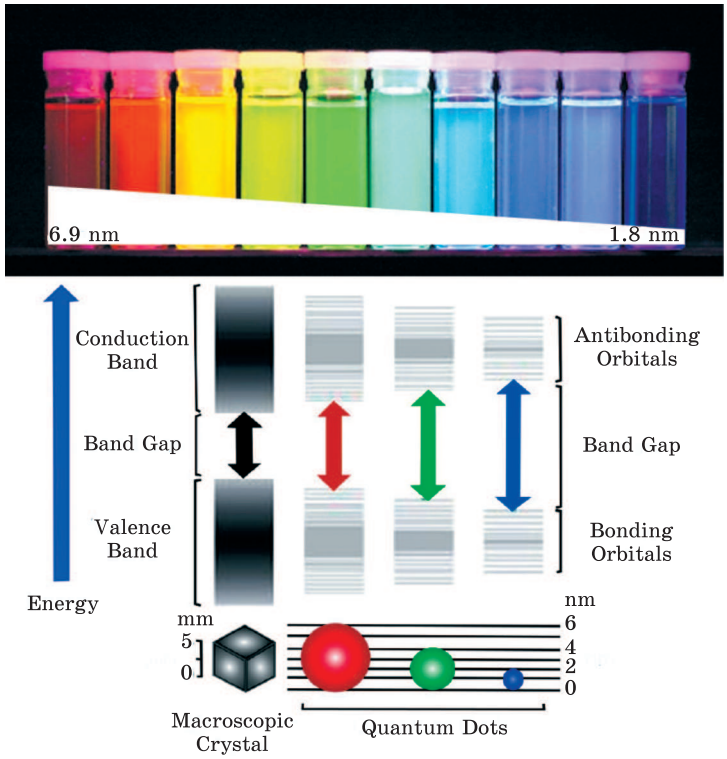

Fig. 20. The quantum dots of CdSe/ZnS core/shell, where CdSe core diameters vary in the range of 1.8–6.9 nm (above), and the change in the band gap value *vs*. the nanocrystal size (below) [51]

particles 2–10 nm in size containing 10^3–10^5 atoms (quantum dots). Such structures are being created based on inorganic semiconductor mate-rials (Si, PbSe, InP, CdSe, *etc*.) coated with a monolayer of a stabilizer from organic molecules (see Fig. 20, review [51] and references therein).

The most easily realized shape of the quantum dot is the sphere. However, there are also ellipsoidal (nanorods) quantum dots, as well as nanocrystals with a complex architecture, *e.g.*, tetrapods. In addition, the doping of quantum dots, the formation of solid solutions of semiconductors as well as the creation of heterojunctions are widely used when the core of a quantum dot is formed from one semiconductor and the shell from another one.

The ability to vary the size of quantum dots, their shape and component composition holds great promise for using such structures for absorption the light in the wavelength range from ultraviolet to infrared. Theoretically, 64% efficiency of solar cells using quantum dots can be achieved [52].

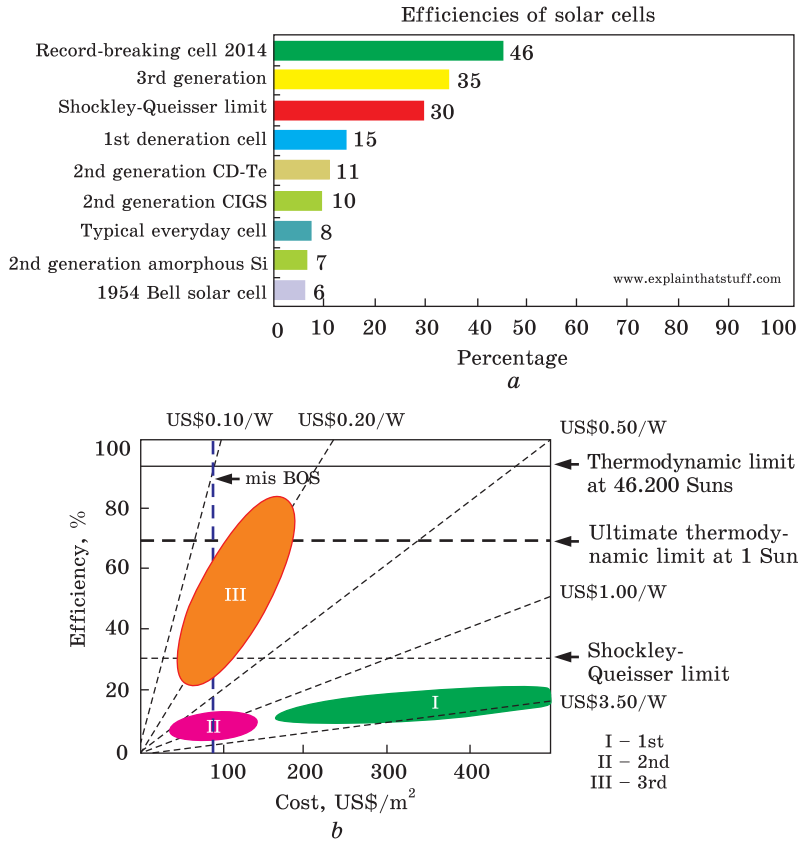

Fig. 21. The efficiency of conversion of solar energy by photocells of the 1st, 2nd, and 3rd generations (*a*), and the efficiency-cost trade-off for the three generations of solar cell technology (*b*) [53]

Fig. 21 shows how the efficiency of solar radiation conversion increased when using photocells of 1–3 generations and the change in economic benefits from their use.

Nanomaterials in Hydrogen Energy

Humanity throughout its historic existence consistently absorbed more and more energy-efficient sources of energy: wood, coal, oil, and gas. The energy intensity of this fossil fuel is determined by the percentage content of hydrogen in the hydrocarbon molecule (Fig. 22).

The most advantageous is to use hydrogen in a 'pure' form. However, in order to realize this advantage, it is necessary that hydrogen react with oxygen in the ionized state. Only then, the released energy would be almost three times more than from the combustion of gasoline, methane or methanol, *e.g.*, in internal combustion engines. At present, sev-

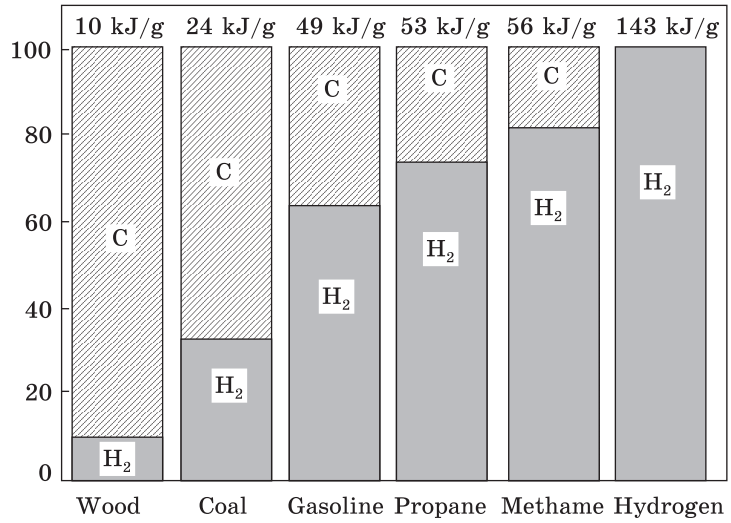

Fig. 22. Comparative data on the specific energy intensity of various fuels [54]

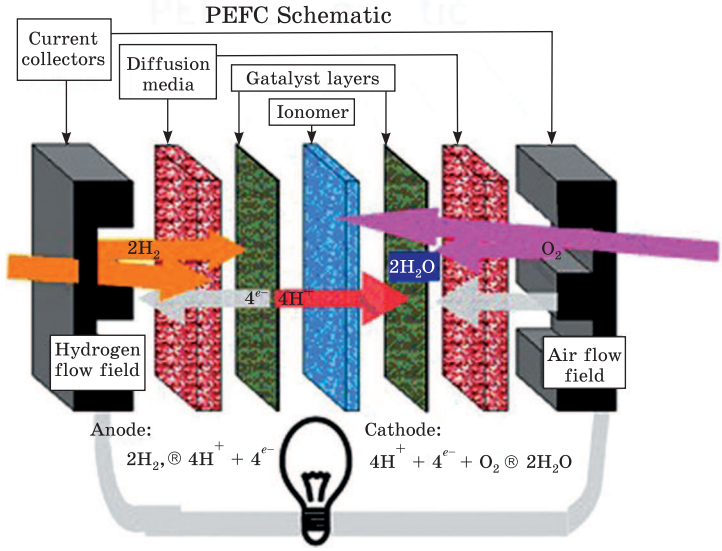

Fig. 23. Hydrogen fuel cell [55]

eral types of solid-state electrolytes (proton exchange membrane, PEM) have been developed that ensure the reaction between hydrogen and oxygen ions in a hydrogen fuel cell (Fig. 23). Their performance today dictates the temperature range (300–400 K) and pressures (0.1–3.0 MPa), within which the hydrogen absorption/desorption should be carried out.

The main problem that hinders the development and use of electrical installations working on hydrogen fuel is the lack of materials capa-

ble of accumulating hydrogen in large quantities. In the early 21st century, the U.S. Department of Energy (DOE) formulated the basic requirements for the fuel systems of cars, which are adjusted and refined every year [56]. In particular, the minimum amount of hydrogen that can be accumulated in the storage tanks must be at least 6 wt.% of the mass of the storage system itself.

Hydrogen in solids can be absorbed in the form of hydrides in dense structures and in the molecular state in porous materials. There are hydrogen storage devices, in which hydrogen is retained in the crystal lattice in both the atomic and molecular states. In porous materials, the interaction between hydrogen molecules and pore surfaces is due to the weak Van der Waals forces (physical adsorption or physisoption). The heat of adsorption for various materials is in the range of 3–7 kJ/mol. As a result, most of the hydrogen absorbed by the pores is desorbed at temperatures up to 77 K. At room temperature, not more than 2 wt.% H_2 is released [57]. Hydrogen in hydrides is in the atomic state and forms chemical compounds with atoms of the crystal lattice (chemical adsorption or chemisorption). The heat of chemical adsorption for conventional polycrystalline structures exceeds 50 kJ/mol. This complicates the hydrogen desorption from hydrides at temperatures <500 K [58]. To ensure the hydrogen release to occur in the temperature range 300–400 K, the desorption heat value should be in the range of 27–50 kJ/mol.

Accumulation of Hydrogen in Porous Structures

Nanocrystalline Carbon. In the mid-1980s, a new class of carbon nanostructures termed fullerenes was first synthesized. Numerous studies of this material stimulated the appearance in 1991 of several new modifications of fullerenes: single-walled and multi-walled nanotubes, nanofibres (Fig. 24). The features of formation of a carbon nanostructure determine its unusual properties (see, *e.g.*, reviews [60–62] and references therein). Despite the low density (1.3–1.4 g/cm^3), carbon nanostructures have high strength—up to 48000 kN·m/kg (for comparison, carbon steel has 154 kN·m/kg). The Young's modulus of single-walled and multi-walled tubes varies in the range of 800–1000 GPa (for carbon steel, 200 GPa). Standard single-walled tube withstands the pressure up to 24 GPa without deformation.

Carbon nanoporous structures that can absorb hydrogen by physical adsorption also include activated carbon (AC). The specific surface area in such a material can vary in the range of 1000–4000 m^2/g.

At present, it is generally accepted that only two processes are responsible for the adsorption of hydrogen by carbon nanoporous structures, *viz.*, adsorption either on the surface of pores or inside the pore volume. In both cases, the specific surface area and pore volume are

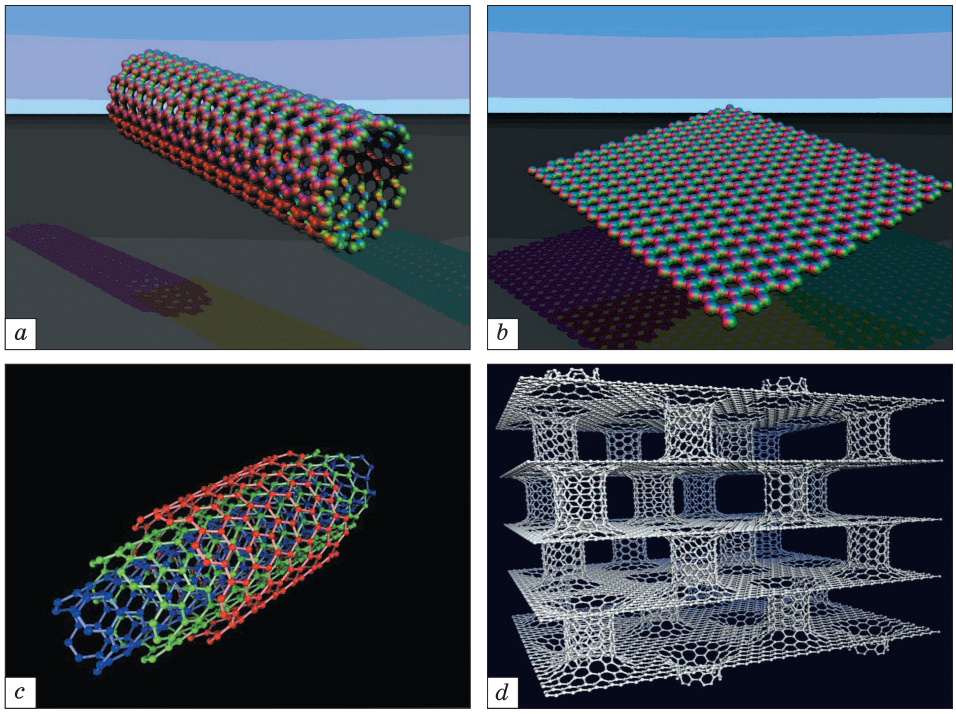

Fig. 24. The examples of nanostructured carbon: (*a*) a single-walled nanotube (SWNT); (*b*) an one-atom-thick sheet of carbon—graphene; (*c*) a multi-walled nanotube (MWNT); and (*d*) a multi-sheeted framework structure, which consists of carbon nanotubes and graphene sheets combined in order to form a three-dimensional network nanostructure (see, *e.g.*, [59–62] and references therein)

important adsorption characteristics. In addition, taking into account the size of the hydrogen molecule (0.29 nm), an important characteristic of the adsorption capacity is diameter and shape of the pores.

Considerable interest in nanoporous carbon-based structures was largely determined by the results the research carried out by A. Dillon *et al.* [63] in 1997. It was revealed that such materials could absorb hydrogen in quantities sufficient for their practical use. However, numerous experimental studies carried out undertaken later showed that the situation was less promising due to the wide scatter in the results obtained by different researchers for the same materials.

Nevertheless, nowadays, it is possible to summarize some of the regularities in hydrogen absorption by various nanoporous carbon structures. A common feature for all structures is the low temperature of the maximum hydrogen adsorption regardless of the surface area of the pores that is stipulated by the physical mechanism of adsorption. It was shown [64] that activated graphite AX-21 with a specific surface area of 2800 m^2/g absorbed the greatest amount of hydrogen exactly at

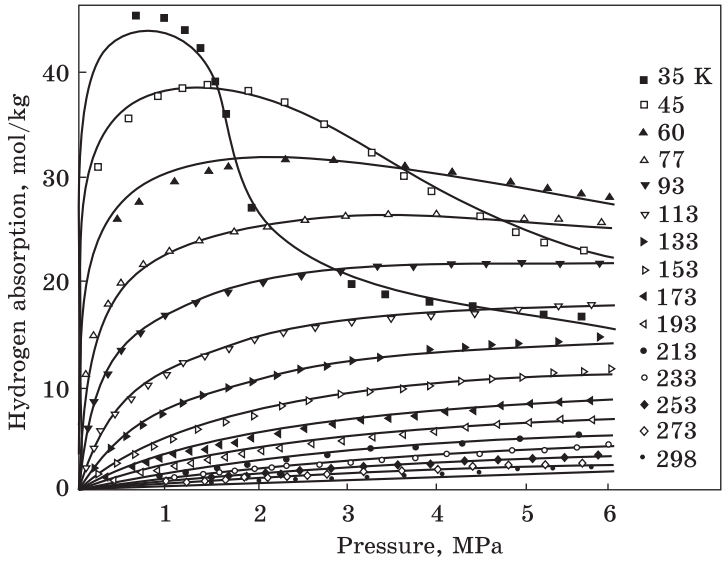

Fig. 25. Isotherms of hydrogen adsorption by activated graphite AX-21 [64]

such temperatures while absorption at room temperature was insignificant (Fig. 25).

Analysing the numerous results on the absorption of hydrogen by nanotubes, nanofibres and nanoporous activated carbons [65], it is difficult to reveal any regularity connecting the value of the specific surface of pores (SBET) with the absorbed hydrogen mass (wt.%). It was shown that the maximum hydrogen amount that can be absorbed at room temperature was 1 wt.%, and this value could reach 2 wt.% at 77 K. These low values of the gravimetric capacitance of nanocarbon structures are explained by the fact that not all pores are able to absorb hydrogen effectively. This explanation is based on the results [66], where it was shown that the optimal size of slit pores that provided good hydrogen adsorption should be 0.6 nm. A good ability to absorb hydrogen is also inherent in the tubular single-walled pores with an internal diameter of 1.3 nm and a distance between the tubes of 0.6 nm [67]. In addition, the absorption capacity of carbon structures may be enhanced through the fragmentation of the porous structure and creation of the additional adsorption centres.

The authors [68] attempted to modify the structure of carbon materials by creating additional sites for the adsorption of molecular hydrogen in the form of packing defects and vacancies. Ball-milling of graphite took place for 80 hours in an atmosphere of hydrogen at 1.0 MPa. Studies have revealed a significant (up to 7.4 wt.%) increase in hydro-

gen adsorption with a simultaneous catastrophic growth in the desorption temperature of it up to 600 K.

Palladium can be used as the catalyst that increases the adsorption capacity of carbon structures. Mixing nanotubes with palladium increases the adsorption capacity three-fold [69]. The observed effect was explained by the distribution of hydrogen between the additional defects formed at the sites of the palladium atom deposition on the walls of the tubes. However, since the initial characteristics of the material were poor (0.1 wt.% H_2), the relative adsorption growth turned out to be so noticeable. An increase in desorption heat of hydrogen (up to 11 kJ/mol) of activated carbon was also observed when a catalyst was added as carbide-forming metal: Ti [70], Li (up to 21 kJ/mol), and K (up to 11 kJ/mmol) [71].

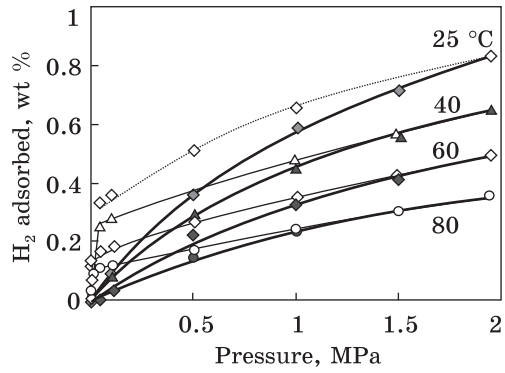

Fig. 26. Isotherms of hydrogen adsorption of doped porous carbon, where shaded (unshaded) symbols relate to adsorption (desorption) [72]

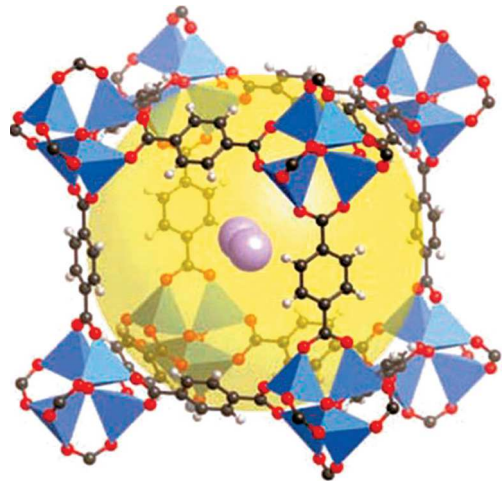

Fig. 27. The structure of MOF-5: $Zn_4O(O_2C–C_6H_4–CO_2)_3$, where triangles denote zinc, small spheres—oxygen, hexagons—organic bunch. The large sphere is the central pore within the cell [73]

Remarkable data indicating a change in the adsorption mechanism in doped nanoporous carbon were obtained in [72]. The material examined in the study has the specific surface area of pores of 2450 m^2/g, and 70% of the pores were smaller than 2 nm. Before saturation with hydrogen, the material was treated in an aqueous solution of phosphoric acid, and then in KOH. This material adsorbed up to 0.8 wt.% H_2 at room temperatures and at pressures below 2 MPa. The distinctive feature was that adsorption–desorption curves exhibited pronounced hysteresis. For all temperatures, a delay in hydrogen release was observed (Fig. 26). The results support the hypothesis that the change of the interaction efficiency of hydrogen molecules with carbon is due to the polarization effect.

Thus, the analysis shows that carbon nanostructures without additional processing cannot hold hydrogen in sufficient quantities at room temperature. In order to improve the adsorption characteristics of nanoporous carbon structures, it is proposed to introduce catalysts in the form of metal atoms in combination with intensive grinding in a hydrogen environment. This treatment stimulates the appearance of additional sites for the adsorption of molecular hydrogen as well as the formation of C–H covalent bonds.

Metal–Organic Framework Structures. Metal–organic framework structures (MOFs) are a special class of porous materials that have long been used for adsorption and separation of gases as well as in heterogeneous catalysis. These materials are created using special chemical methods, which include the slow crystal growth from the heated molten metal oxide and organic substances. Structurally, they represent an organic framework with the ions or clusters of metals in the nodes connected by organic chains (ligands) (Fig. 27).

Since the metal–organic framework is as open as possible, the specific surface area of MOF-structures generally exceeds 1000 m^2/g, and the pore size is typically less than 2 nm. The distances between organic and inorganic components are small, so the strength of MOF-structures is very high. These characteristics determine the prospects of wider application of these materials in the hydrogen storage devices.

In 2003, MOF-5 and MIL-53 framework structures with inorganic constituents Zn^{2+}, Al^{3+} and Cr^{3+} ions were studied [74, 75]. Fig. 28 shows the typical MOF-5 hydrogen absorption isotherms for different temperatures [76].

The isotherm for 77 K is typical for an adsorbent that absorbs hydrogen in a molecular form (physisorption) when a significant increase in the adsorbed gas occurs at low pressures. The maximum saturation at 2 MPa corresponds to ≅4.5 wt.%. Due to the small values of physical adsorption heat in the framework structures, the slope of the curves and the maximum of absorbed hydrogen decrease with the temperature growth. Only 0.1 wt.% is absorbed at room temperature and 2MPa.

Considering that a large number of MOF structures have been investigated to date, the results of the studies can be systematized [77] (see Table 1). The analysis shows that at 77 K, as the volume and specific surface area of the pores increase, the total amount of absorbed hydrogen grows up, regardless of the composition and structure of the material (Fig. 29).

For instance, some structures with pore volume more than 1.5 $cm^3 \cdot g^{-1}$ absorb hydrogen in a large amount: 6.1 wt.% (MIL-101) [78], and 6.7 wt.% (IRMOF-20) [79]. This means that more than 80% of the volume of these structures is free. To enhance the hydrogen capacity of such structures, a further increase in the pore volume and surface area is required but this way is unrealistic.

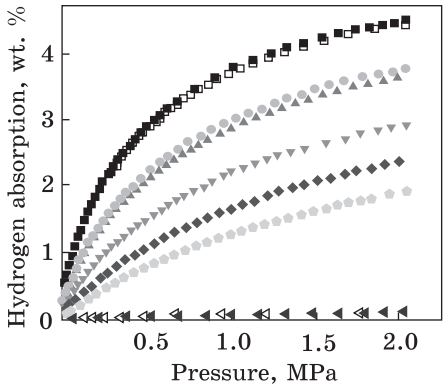

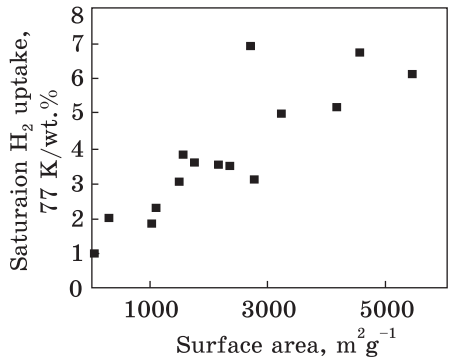

Fig. 28. Isotherms of hydrogen adsorption by the MOF-5 structure [76]

Fig. 29. Correlation between the surface area of MOF structures and saturation hydrogen uptake at 77 K [77]

Thus, despite the optimistic parameters of porosity in MOFs, the kinetics of hydrogen desorption from them is in doubt. The achieved values of the surface area of the pores allowed to accumulate the hydrogen amount needed today. However, these values are limiting for this class of materials. In addition, due to the large difference in the size of the hydrogen molecule and the diameter of the main pores in the MOFs, it is difficult to expect that it will be possible to keep the desired hydrogen amount in them at room temperature.

Therefore, the focus of researchers is to develop the structures with pores <0.6 nm in size, and to create conditions under which the partial dissociation of hydrogen molecules and the formation of chemical compounds would become possible. Ideally, all hydrogen molecules should interact with adsorption centres (pore walls). To hold a sufficient amount of hydrogen at room temperature, the porous structure must consist of pores of minimum size with the maximum total surface area.

An impregnation of the central pore with a stable inorganic structure, for example, fullerene C_{60} can be one response to this problem [80]. The pore diameter in the MOF-177 structure is 1.18 nm, which is enough to accommodate the C_{60} molecule in it (Fig. 30).

As expected, an increase in the weight of the MOF-177 frame by add-

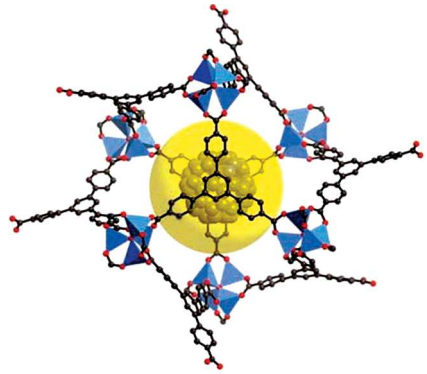

Fig. 30. The configuration of MOF-177 frame structure with an embedded C_{60} molecule [80]

ing a carbon structure will be compensated by the growth in the hydrogen adsorption capacity. In order to reduce the pore size, it is also proposed to create frame structures in which the nodes of one cell penetrate at the central pore of the neighbouring cell, thereby reducing its diameter. In this process of catenation, the mutual penetration of identical frameworks into each other is possible as well as embedding a smaller frame within a frame with a larger diameter [81].

Data on the transformation of IRMOFs structures by placing additional frameworks inside the initial cells has already been published. This process leads both to an increase in the adsorption capacity at 77 K and to absorption of more than 1 wt.% at room temperature and 48 bar pressure [82].

Accumulation of Hydrogen in Hydrides

Magnesium Hydride. Hydrogen can form hydrides with more than 90 elements of periodic (Mendeleev) table. Moreover, hydride-forming alloys and complex hydrides are available in great amounts. Unfortunately, none of these original hydrides meets requirements set to solid-state hydrogen accumulators [83]. The vanadium (VH_2) and palladium ($PdH_{0.6}$) hydrides are the most preferable. However, the desorption temperature of vanadium nitride is somewhat lower and palladium is a rather expensive material and it accumulates hydrogen in insufficient amounts; but still, generally, the hydride adsorbing capacity is sufficiently high.

Another area of focus is magnesium hydride (MgH_2). It has the highest energy density of 9 mJ/kg, a good rated hydrogen capacity of 7.7 wt.%, low cost and a good reproducibility of results [84, 85]. Its main drawbacks are high desorption temperature, low hydrogen release kinetics and low air and oxygen reactivity [86, 87]. A decrease in desorption temperature can be reached through a reduction of the size of MgH_2 particles, which, in turn, increases the hydrogen diffusion coefficient. The hydrogen release kinetics can be improved through the creation of catalytic centres on the surface of magnesium hydride particles. These centres accelerate the dissociation of hydrogen molecules. The poisoning effect of granular boundaries created by magnesium hydride can be reduced through the implantation into the boundaries of the elements, which are more active with regard to oxygen.

The main method, which is used today for the creation of hydride storages of hydrogen, provides milling of powder material in ball mills in the atmosphere of inert gas or hydrogen. An increase in the milling time results in the reduction of the size of particles and in the increase of the area of their surface. The surface area, as well as its configuration and purity, are the critical parameters that influence the kinetics of hydrogen

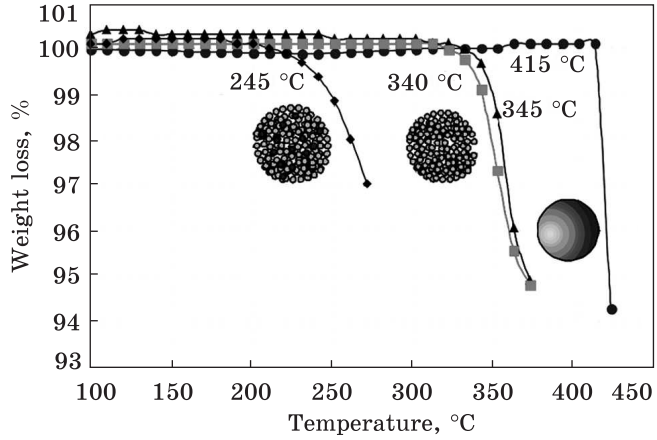

Fig. 31. Thermogravimetric weight loss profiles *vs.* desorption temperature and degree of MgH_2 milling: • — commercial MgH_2; ▲ — MgH_2, 9 hour ball milling; ■ — MgH_2, 12 hour ball milling; ◊—MgH_2, 9 hour ball milling + 10 mol.% nanocatalyst [88]

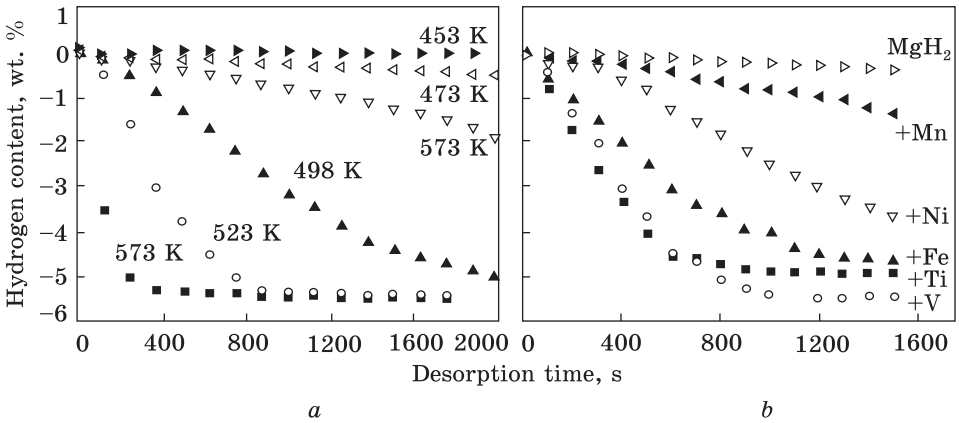

Fig. 32. Hydrogen desorption curves for mechanically milled MgH_2–5 at.% V (*a*) [92] and MgH_2–5 at.% *M* (*M* = Ti, V, Mn, Fe, Ni) at 523 K and 0.015 MPa (*b*) [89]

adsorption. It was shown that the temperature of hydrogen desorption considerably decreases after long-time milling (10 and more hours) and the rate of adsorption/desorption increases (Fig. 31) [88]. However, the milling time has no implications for the adsorbed hydrogen quantity.

Even small amounts of catalysts being added to magnesium hydride during milling results in the developing a large number of defects on the MgH_2 grains surface, which initiate the hydrogen dissociation. Such metals as V and Ti hamper oxidation processes during multiple adsorption/desorption reiteration [89]. In order to decrease the temperature of hydrogen desorption from magnesium are proposed to mix it with the metals having hydrides with low desorption heat. The addition of Pd, Ni and Ge is entailed in improvement of kinetic characteristics of MgH_2. For instance, the presence of Ge decreases the hydride decomposition temperature in a range from 50 to 150 °C, depending on the Ge amount

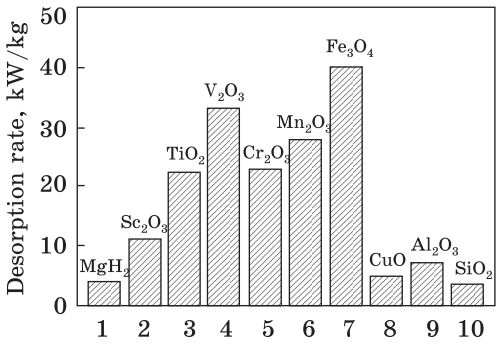

Fig. 33. Desorption rates for various MgH_2/M_xO_y (M is a metal) systems at 300 °C [96]

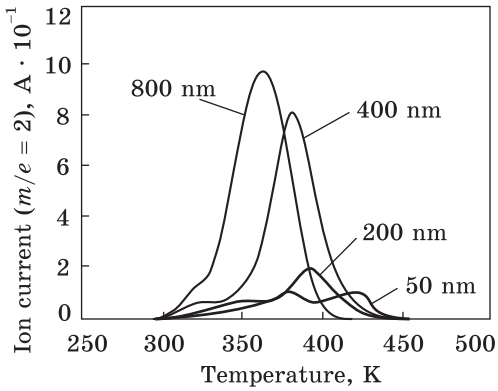

Fig. 34. TDS spectra of several hydrogenated Pd/Mg(*x* nm)/Pd films [97]

[90]. However, this effect disappears after several adsorption–desorption cycles. Numerous studies relate to the MgH_2–V system [91–94]. It has been shown that vanadium produces a positive impact on the dissociation of hydrogen molecules. The addition of 5 at.% of vanadium significantly contributes the hydrogen capacity of magnesium without changing the thermodynamic properties (Fig. 32, *a*) [92]. Moreover, as it was revealed by Dehouche *et al.* [88], MgH_2–5 at.% V composite has high cycle stability.

A comparative analysis of transition metals influence on adsorption characteristics of MgH_2 composite showed that vanadium and titanium may be regarded as the most efficient catalysts (Fig. 32, *b*) [89].

Kinetics problems with MgH_2 can be improved through the addition of oxides [91, 95, 96]. A presence of oxide particles during milling contributes to the formation of defects on the surfaces of MgH_2 particles making the hydrogen dissociation easier. Presence of Cr_2O_3 accelerates hydrogen adsorption; V_2O_5, Mn_2O_3, and Fe_3O_4 accelerate desorption (Fig. 33) [96]; Al_2O_3 and Cr_2O_3 considerably increase the amount of adsorbed hydrogen up to 4.09 and 4.02 wt.%, respectively [95].

In order to analyse comprehensively the opportunities for using magnesium as a hydrogen adsorbent, the attention should be paid to the research of the adsorption properties of thin-film magnesium-based structures. These types of structure of are alternatives to nanocrystalline powder materials. Their thermodynamic stability can be worse and desorption temperature lower in comparison with those of magnesium hydride. Their thickness and grain size can be varied in a wide range. This provides a good opportunity to study the relationship between the film structure and its thermodynamic and kinetic properties.

The basic idea of experiments is to sputter the multilayer films where magnesium layers are in contact with the layers of other metals

M [97, 98] or with single-layer multicomponent Mg_xM_y films [99, 100], which, in both cases, should facilitate the hydrogen dissociation and improve the adsorption kinetics.

In Refs. [97, 98], palladium was selected as the second material for the multilayer films. Palladium has lower adsorption capacity and desorption temperature in comparison with magnesium. It has been revealed that the presence of palladium in a double-layer Pd/Mg film allows magnesium to absorb more than 5 wt.% of hydrogen at 373 K and 0.1 MPa, which means that palladium acts as a catalyst. Magnesium film with the same experimental characteristics adsorbed no hydrogen. It has been also shown that the hydrogen adsorption kinetics relied heavily on the parameters of film deposition. The metal sputtering that contributed to the formation of nanocrystalline columnar structure provided the opportunity to reduce the desorption temperature.

Fig. 34 depicts the thermal desorption spectroscopy (TDS) data on H adsorbed by the three-layered Pd(50 nm)/Mg(x nm)/Pd(50 nm) film, where the magnesium film thickness x varied in the range of 50–800 nm [97].

In light of information on thermal desorption data, film thickness, and its specific mass, Mg film thickness has no effect on the hydrogen content, which was approximately the same ($\cong$5 wt.%) in all magnesium films. An increase in the film thickness positively influenced the thermodynamics of hydrogen desorption. The hydrogen desorption temperature was about 360 K at the maximum thickness of studied magnesium films.

Nitrogen-Containing Complex Hydrides. The fact that nitrogen-containing metal hydrides can absorb large hydrogen amounts was discovered by accident after thermal treatment of lithium-containing nanotubes in nitrogen atmosphere [101]. Diffraction analysis of hydrogen-saturated nanotubes revealed the presence of $LiNH_2$ and LiH compounds. Further studies have shown that initially nitrogen forms Li_3N, and then the hydrogen addition leads to the reaction

$$Li_3N + 2H_2 = Li_2NH + LiN + H_2 = LiNH_2 + 2LiH. \quad (3)$$

Because of this reaction, the hydrogen uptake can reach up to 10.5 wt.%. According to thermodynamic analysis, the adsorption heats of $LiNH_2$ + + 2LiH and Li_2NH + LiN are 80 and 66 kJ/mol, respectively [102].

Numerous studies of the absorptive capacity of materials containing not more than one metal have shown that hydrogen retention occurs only due to the chemical adsorption, which heat is in the range of 40–90 kJ/mol. The temperature range of the hydrogen desorption is 250–500 °C. The amount of absorbed hydrogen can reach 7 wt.% but it releases mainly as ammonia rather than as an atomic hydrogen [103].

To reduce the desorption temperature, either the complex hydrides with two or more metal components are produced [103–106] or boron-containing hydrides are added [101]. In this cases, the amount of ab-

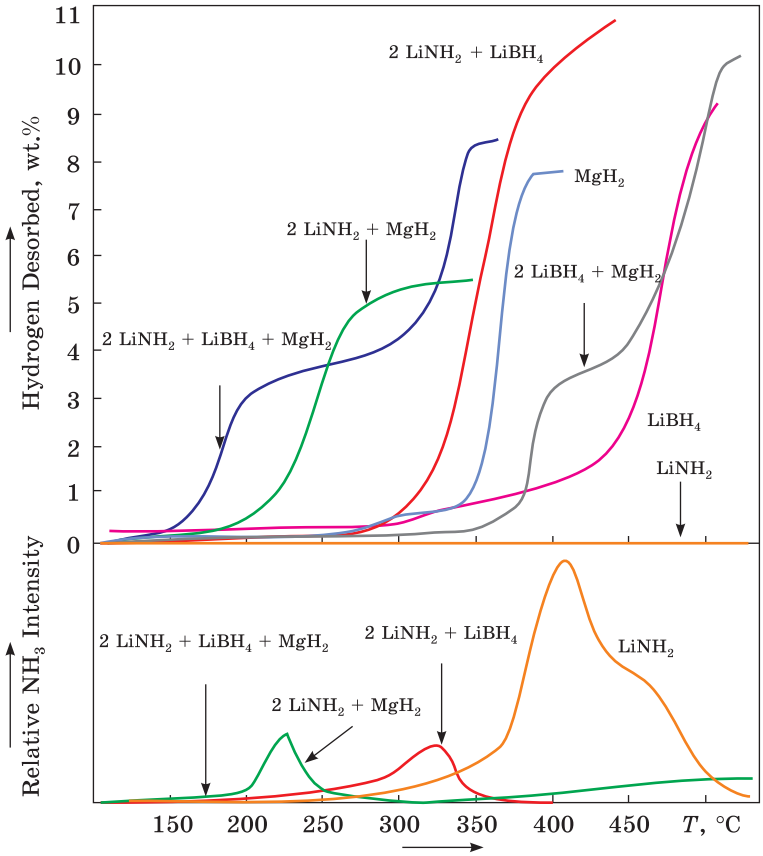

Fig. 35. Hydrogen (top) and ammonia (bottom) kinetic desorption data as a function of temperature (5–550 °C) for the ternary composition along with its unary and binary constituents (see [107] and references therein)

sorbed hydrogen remains quite large, and desorption temperature can be slightly reduced down to 150–200 °C (Fig. 35) [107].

Analysis of a large number of studies shows that the decrease in the heat of hydrogen desorption comes mainly from the creation of multicomponent systems based on light metals: Li, Mg, Ca, Na containing nitrogen and boron hydrides, and grinding the hydride grains. These techniques inevitably lead to an increase in the degree of defectiveness of the material and a decrease in the size of intergranular pores. It can be expected that part of the molecular hydrogen will be accumulated in the created pores and vacancy-type defects. As a result, a decrease in the heat of adsorption will lead to a decrease in the desorption temperature.

Hydrogen Accumulation by Complex Hydrides VN_x–H_y and TiN_x–H_y

Analysing the above results, the two main lines of research can lead to a significant increase in the adsorption properties of hydrogen storage devices. The first line relates to attempts to transform the porous structure of the metal–organic framework and carbon nanomaterials by adding alloying components. This approach, on the one hand, should provide a reduction in the average pore size, and, on the other hand, promote the dissociation of some hydrogen molecules and the retention of the atoms through the formation of chemical bonds with carbon, oxygen, or metal.

The second line is related to the change of the composition and structure of hydride-forming materials by increasing the number of metal components, mixing nitrogen and boron-based phases, or intensifying the degree of grinding in ball mills. All these processes lead to the greater defectiveness of structure, to less grain size, and to the formation of a system of intergranular nanopores that will capture the molecular hydrogen. That means that such structures are able to absorb hydrogen not only by the formation of chemical compounds but also because of its physical adsorption.

Therefore, attempts to create materials capable of absorbing hydrogen due to both physical and chemical adsorptions are very reasonable. All these requirements can be met by the nanocrystalline materials with intergranular joints containing nanopores, and the grain boundaries provide rapid hydrogen absorption by the crystal lattice and pores as well as its release.

In our previous studies [108], it was shown that nanocrystalline porous structures can be obtained using the ion-beam assisted deposition (IBAD) method. Film deposition at the bombardment with high-energy nitrogen and helium ions promotes the formation of a nanocrystalline porous structure (grain size is of 20–50 nm). Fig. 36 displays the SEM images of the VN_x–H_y film in the initial state and saturated with hydrogen at 0.3 MPa [109]. Initially, the films consist of disordered non-equiaxial particles. The particles of the cylindrical shape are of 50–70 nm in length with a diameter of 10 to 15 nm. Hydrogen-saturated films acquire a round shape and their diameter varies in the range of 30–100 nm. The analysis of the selected area electron diffraction (SAED) patterns of the initial and hydrogen-saturated films revealed an f.c.c. structure of vanadium nitride.

Hydrogen absorption isotherms are similar for all samples (Fig. 37). The knee of the curves more evident with the temperature growth is observed for TiN_x–H_y films at 0.1–0.125 MPa. This can be caused both by the successive filling the traps of various activity by hydrogen and

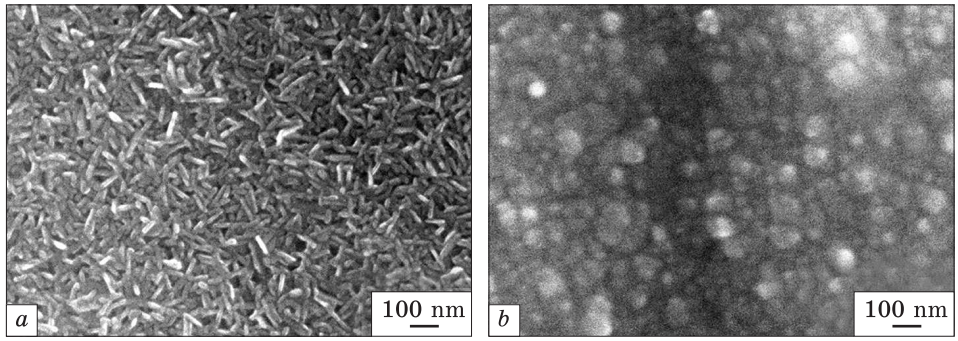

Fig. 36. The structure of VN_x–H_y films in the original state (*a*) and after the hydrogen saturation (*b*) [109]

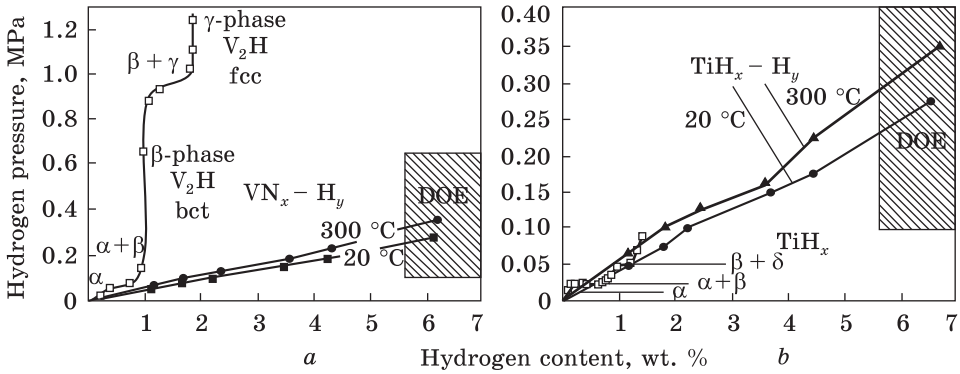

Fig. 37. Pressure *vs*. the hydrogen content for VN_x–H_y (*a*) and TiN_x–H_y (*b*) films [109] along with their constituents VH_x [110] and TiH_x [111, 112]

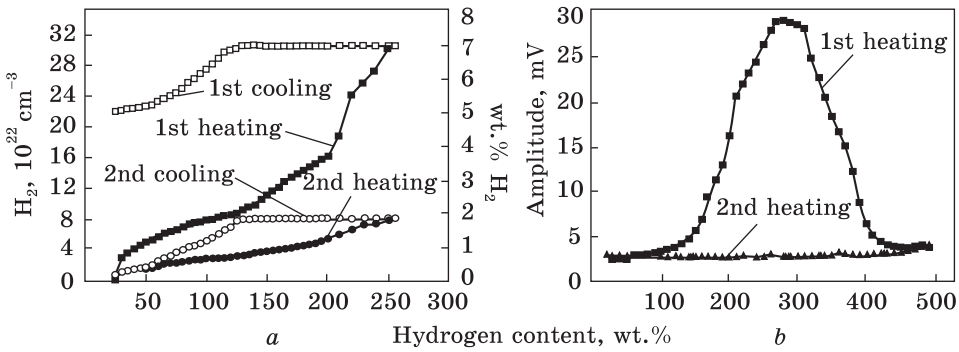

Fig. 38. Amount of released hydrogen *vs*. the annealing temperature for VN_x–N_y film (*a*), and hydrogen desorption spectra of VN_x–N_y film (*b*) [113]

the penetration of hydrogen into the film structure accompanied by the chemical compound formation. It is important to note that vanadium and titanium nitrides exhibit approximately the same activity with re-

spect to hydrogen. This indicates that the significant portion of hydrogen is absorbed by the porous structure that is inherent in both nitrides. It is noteworthy that the amount of absorbed hydrogen and the pressure of hydrogen saturation meet the requirements of DOE.

Fig. 38, *a* shows the dependence of the released hydrogen amount on the annealing temperature for the VN_x–H_y film [113]. The films were annealed in a closed vacuum chamber. As can be seen from the curves, the hydrogen desorption begins just at 30–50 °C. At 200 °C, the amount of molecules of desorbed hydrogen reaches $1.5 \cdot 10^{19}$ (or 3.5 wt.%). A further temperature growth causes a rising rate of hydrogen release. At 275 °C, the total mass of the liberated hydrogen exceeds 7 wt.%. Upon cooling below 100 °C, up to 2 wt.% of hydrogen is absorbed by the open porous structure of the films.

Fig. 38, *b* gives the spectra of thermal desorption of hydrogen from VN_x–H_y films showing that hydrogen starts to release at 50 °C, and the maximum desorption rate is observed at 270 °C.

The results demonstrate that the use of IBAD allows not only controlled formation of nanoporosity with given parameters but also to embed this nanoporosity into the nanocrystalline structure of the matrix. Material produced by given technique is capable of accumulating hydrogen at low pressures and room temperature. The availability of broad channels between grains provides the high diffusion mobility than allows accumulating hydrogen and its releasing from the material within a short time period.

Instead of an Afterword

Historians engaged in science studied have noted an interesting timeline. As a rule, the time period between the discovery of a physical phenomenon and its widespread practical application is about 30 years, *e.g.*, the internal combustion engine, textiles, semiconductor, *etc*. As noted above, N. Taniguchi firstly used the term nanotechnology in 1974. Currently, we have a revolution in this area. A. Fujishima described the photocatalytic reaction of water separation using TiO_2 electrode in 1975 [114]. Since then, many studies of this material have been done, most of which concern the nanocrystalline state. Today, TiO_2 is almost the main candidate for use in rechargeable batteries, solar cells and hydrogen production technology [115]. In 1991, it was announced the production of carbon nanotubes. This work has largely prompted the scientists around the world to develop and use the bottom-up method for creating nanostructures. As a result, a large number of promising for use in energy sector objects, namely, carbon-free nanotubes, nanofibres, nanorods, and others have been obtained and investigated.

All energy-generating technologies that were considered in this review are based on three main processes: the generation, transfer, and

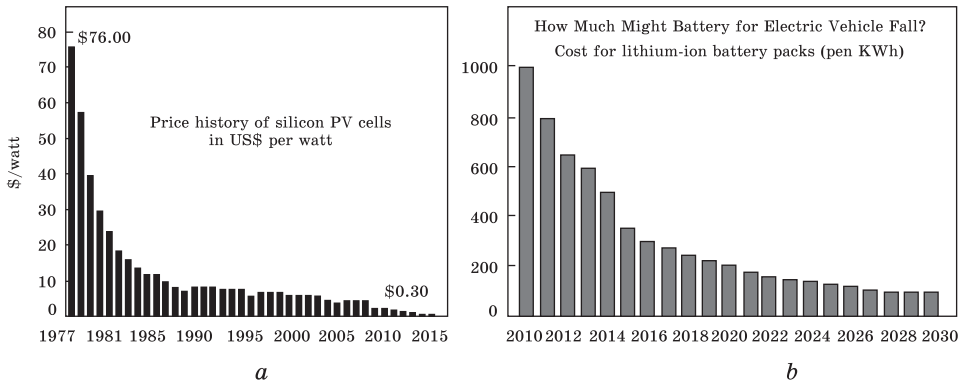

Fig. 39. Dynamics of falling prices for solar cells (*a*) and lithium-ion batteries (*b*) [117, 118]

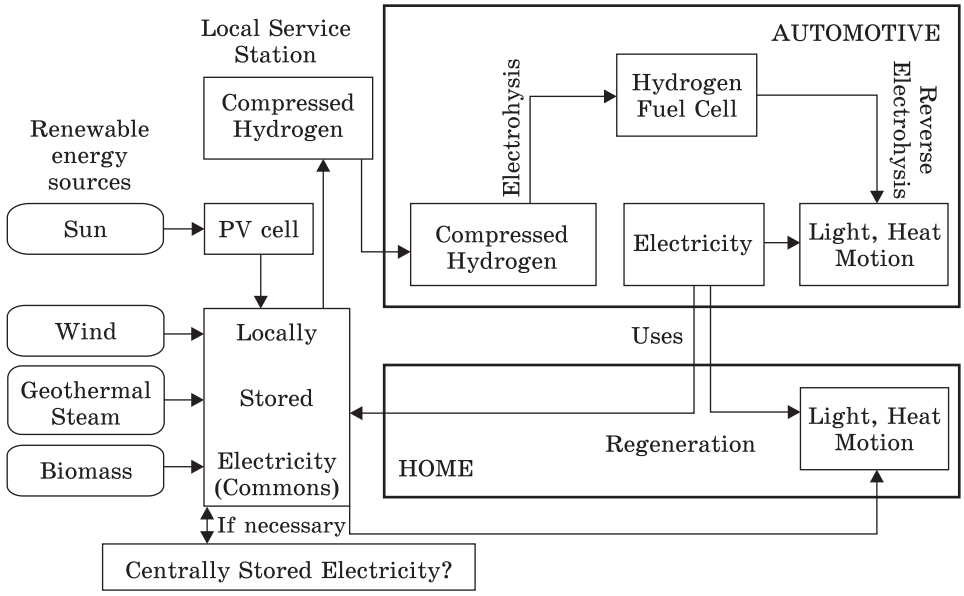

Fig. 40. Using of alternative energy sources in everyday life [119]

accumulation of charged or neutral particles in the lattice of a solid. The generation of charges should be carried out from a large area of the electrode, the transfer must occur in the smallest time interval, and the accumulation of charged particles (atoms) should take place in the most limited volume. The maximum specific energy density can be achieved only if all the listed conditions are met, which, in turn, is possible only in nanocrystalline and/or nanoporous structures.

Therefore, it is clear that, in the last decade, an avalanche-like increase in the number of publications devoted to the creation and use of

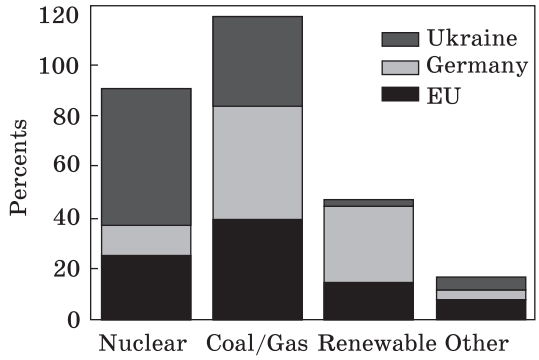

Fig. 41. Energy balance of the EU, Germany, and Ukraine [121, 122]

nanomaterials has been observed. The largest number of publications is from China and the USA. They are followed by India, Germany, South Korea, and Japan. The number of publications on this subject in Ukraine, unfortunately, does not exceed 1% of the total number of articles in the world. Moreover, only 14.5% of articles published in Ukraine are devoted to nanomaterials [116].

In spite of the fact that by the present moment scientists have not yet created nanostructured materials that could be used in industry or in everyday life, there is already a conversion of electric consumers to substituting technologies. This is due to the fact that production technologies, *e.g.*, of solar cells and lithium-ion batteries are constantly improving and becoming cheaper (Fig. 39). As a result, the payback period of products significantly shortens. In addition, a number of governments are encouraging investors by introducing a 'green tariff'.

Formation of a concept for the solar energy use occurs in parallel with a greater share of this energy in the overall energy balance. In particular, the solar panels can become the main source of electricity and heat in everyday life (Fig. 40) [119]. The energy they generate can be spent to produce hydrogen at daylight and to recharge electric cars at night. Wind energy, biomass processing, and geothermal energy can be used additionally to ensure the reliability of energy supply to consumers.

Nowadays, renewable energy has reached the first place in the world in terms of growth in consumer capacity; in 2015, 500 000 solar panels were being installed every day in the world; two wind-power units are installed every hour in China. China generally holds a leading position in terms of investments in alternative energy. China invested the largest amount of money in renewable energy last year, at $126.6 billion. This represents a 31% increase compared to 2016. Moreover, this is understandable because, at present, 65% of the needs for electricity and heat in China are met by coal. It is planned that in 2020, 30 million houses will be provided with energy from solar panels, and the share of replacement energy in the overall energy balance will reach 20%.

World energy is on the verge of a transition from an industrial form to a post-industrial one. This transition can occur in three scenarios: inertial, stagnant and innovative [120].

The inertial scenario, which is based on hydrocarbons, is energy-wasteful. Priorities in the use of energy sources are oil, gas, coal, renewable energy sources (RES), nuclear power (NP). Because of its implementation, a rapid growth in demand for fossil raw materials of all types is inevitable, and, as a result, a significant deterioration in the environmental situation in the world.

The stagnation scenario (oil, gas, coal, RES, NP) implies controlled development near the limits of growth of the industrial phase.

Finally, the innovative scenario (RES, gas, oil, NP, coal) implies a transition from the market of raw materials to the market of services and technologies. Thus, by 2030, a new type of energy can be formed.

Fig. 41 shows comparative data on energy supplies to the EU, Germany, and Ukraine. It can be seen that the priorities of Germany most closely correspond to the innovative way of development. A similar situation exists in England. The energy bias towards nuclear and hydrocarbon energy that was formed in the formerly USSR and inherited Ukraine is doomed to it, rather an inertial scenario.

According to the International renewable energy agency (IRENA), by mid-2015, 164 countries of the world have declared certain national goals for the development of renewable energy. Ukraine is among them. Renewable sources finally ceased to be a niche but became a direction. At the end of 2016 in the world, the total renewable power capacity including and not including hydro was equal to 2017 GW and 921 GW, respectively. Growth in comparison with 2015 was 8.7% (including hydro) and 17.3 % (not including hydro) [120].

Today, there is no doubt that the capital costs and the cost of electricity produced by RES will be reduced. The widespread introduction of nanostructural materials into solar energy, batteries and hydrogen power will significantly accelerate this process. Electricity produced from hydrocarbon fuel will go up.

Unfortunately, on the path to transition to RES, Ukraine takes a passive position. Declared objectives to be achieved through the efforts of Ukrainian science have no financial support since only 0.16% of gross domestic product (GDP) was allocated for financing science, which is not enough to develop even innovation directions. Choosing the path of development of the country and its economy, the government needs to clearly prioritize science, take into account the experience and world trends in energy, and focus on the economies of the advanced countries of the world.

REFERENCES

1. A. Demirbas, *Energy Sources, Part B*, **4**, No. 2: 212 (2009).
2. K.G. Satyanarayana, A. Mariano, and J.V.C. Vargas, *Int. J. Energy Research*, **35**, No. 4: 291 (2011).
3. U. Sahaym and M.G. Norton, *J. Mater. Science*, **43**, No. 16: 5395 (2008).
4. N.S. Lewis, *Science*, **315**: No. 5813: 798 (2007).
5. Y. Sun, N. Liu, and Y. Cui, *Nature Energy*, **1**: 16071 (2016).
6. R.P. Feynman, *Engineering and Science*, **23**, No. 5: 22 (1960).
7. N. Taniguchi, *Proc. of the Int. Conf. on Production Engineering* (Tokyo: 1974), p. 18.
8. D.E. Carlson and C.R. Wronski, *Appl. Phys. Lett.*, **28**, No. 11: 671 (1976).
9. G. Binning and H. Rohrer, *Surf. Sci.*, **126**, Nos. 1–3: 236 (1983).
10. G. Binnig, C.F. Quate, and Ch. Gerber, *Phys. Rev. Lett.*, **56**, No. 9: 930 (1986).
11. S. Iijima, *Nature*, **354**: 56 (1991).
12. T.P. Yadav, R.M. Yadav, and D.P. Singh, *Nanosci. Nanotechnol.*, **2**, No. 3: 22 (2012).
13. H. Gleiter, *Prog. Mater. Sci.*, **33**, No. 4: 223 (1989).
14. R. Birringe, *Mater. Sci. Eng. A*, **117**, 33 (1989).
15. R. Thiruvengadathan, V. Korampally, A. Ghosh, N. Chanda, K. Gangopadhyay, and S. Gangopadhyay, *Rep. Prog. Phys.*, **76**, No. 6: 066501 (2013).
16. J.L. Liu and S. Bashir, *Advanced Nanomaterials and Their Application in Renewable Energy* (Amsterdam: Elsevier: 2015).
17. P. Edwards, R. Johnston, and C. Rao, *Metal Clusters in Chemistry* (Eds. R. Braunstein, L. Oro, and P. Raithby) (Weinheim: Wiley-VCH: 1999), vol. **3**, p. 1454.
18. N.T. Gladkih, S.V. Gukarov, A.P. Kryshtal, V.I. Larin, V.N. Suhov, and S.I. Bogatyrenko, *Poverkhnostnye Yavleniya i Fazovye Prevrashcheniya v Kondensirovannykh Plenkakh* [Surface Phenomena and Phase Transformations in Condensed Films] (Kharkiv: KhNU: 2004) (in Russian).
19. K.T. Lee and J. Cho, *Nano Today*, **6**: 28 (2011).
20. Y.G. Guo, J.S. Hu, and L.J. Wan, *Adv. Mater.*, **20**, No. 15: 2878 (2008).
21. R. Morris, B. Dixon, T. Gennett, R. Raffaelle, and M.J. Heben, *J. Power Sources*, **138**: 277 (2004).
22. Z. Zhou, J. Zhao, X. Gao, Z. Chen, J. Yan, P. von Rague Schleyer, and M. Morinada, *Chem. Mater.*, **17**, No. 5: 992 (2005).
23. H. Xie, Y. Li, S. Jin, J. Han, and X. Zhao, *J. Phys. Chem. C*, **114**, No. 21: 9706 (2010).
24. M.S. Wu and R.H. Lee, *J. Power Sources*, **176**, No. 1: 363 (2008).
25. G. Zhang, L. Yu, H.E. Hoster, and X.W. Lou, *Nanoscale*, **5**, No. 3: 877 (2013).
26. J. Chen, X.H. Xia, J.P. Tu, Q.G. Xiong, Y.X. Yu, and X.L. Wang, *J. Mater. Chem.*, **22**, No. 30: 15056 (2012).
27. A.R. Armstrong, G. Armstrong, J. Canales, and P.G. Bruce, *Angew. Chem. Int. Ed.*, **116**, No. 17: 2336 (2004).
28. A. Armstrong, G. Armstrong, J. Canales, and P.G. Bruce, *Adv. Mater.*, **17**, No. 6: 862 (2005).
29. M.C. Yang, Y.Y. Lee, B. Xu, K. Powers, and Y.S. Meng, *J. Power Sources*, **207**: 166 (2012).
30. J. Luo, X. Xia, Y. Luo, C. Guan, J. Liu, X. Qi, C.F. Ng, T. Yu, H. Zhang, and H.J. Fan, *Adv. Energy Mater.*, **3**, No. 6: 737 (2013).
31. H. Wang, D. Ma, X. Xuang, Y. Huang, and X. Zhang, *Sci. Rep.*, **2**: 701 (2012).

32. X. Li, Y. Chen, H. Yao, X. Zhau, J. Yang, H. Huang, Y.-W. Mai, and L. Zhou, *RSC Advances*, **4**: 39906 (2014).
33. S. Guo, J. Liu, S. Qiu, Y. Wang, X. Yan, N. Wu, S. Wang, and Z. Guo, *Electrochim. Acta*, **190**: 556 (2016).
34. P. Bruce, B. Scrosati, and J.-V.Tarascon, *Angewandte Chemie*, **47**, No. 16: 2930 (2008).
35. C. Delmas, M. Maccario, L. Croguennec, F. Le Cras, and F. Weill, *Nature Mater.*, **7**: 665 (2008).
36. R. Malik, D. Burch, M. Bazant, and G. Ceder, *Nano Lett.*, **10**, No. 10: 4123 (2010).
37. D. Wang, H. Buga, M. Grouzet, G. Deghenghi, T. Drezen, I. Exnar, N.-H. Kwon, J. H. Miners. L. Poletto, and M. Graszel, *J. Power Sources*, **189**, No. 1: 624 (2009).
38. J.D. Eppinga and B.F. Chmelka, *Cur. Opin. Colloid Interface Sci.*, **11**, Nos. 2–3: 81 (2006).
39. F. Jiao, K.M. Shaju, and P.G Bruce, *Angew. Chem. Int. Ed.*, **44**, No. 40: 6550 (2005).
40. K. Wong and S. Dia, *J. Energy Resour. Technol.*, **139**, No. 1: 014001 (2016).
41. See https://www.solarwind-sensor.com/wp-content/uploads/2014/04/Silicon-cell-convertible-spectrum.png.
42. S.H. Jensen, P.H. Larsen, and M. Mogensen, *Int. J. Hydrogen Energy*, **32**, No. 15: 3253 (2007).
43. M.D. Kelzenberg, S.W. Booettcher, J.A. Petykiewicz, D.B. Turnet-Evans, E.L. Warren, J.M. Spurgeon, R.M. Briggs, N.S. Lewis, and H.A. Atwater, *Nature Mater.*, **9**, No. 3: 239 (2010).
44. J. Zhu, Z. Yu, G.F. Burkhard, C.M. Connor, Y. Xu, Q. Wang, M. McGehee, S. Fan, and Y. Gui, *Nano Lett.*, **9**, No. 1: 279 (2009).
45. See http://www.rusnano.com/about/press-centre/news/75461.
46. S. Ito, T.N. Murakami, P. Comte, P. Liska, C. Grätzel, M.K. Nazeeruddin, and M. Grätzel, *Thin Solid Films*, **516**: 4613 (2008).
47. H.P. Wu, C.M. Lan, J. Hu, W.K. Huang, J.W. Shiu, Z.J. Lan, C.M. Tsai, C.H. Su, E.W. G. Diau, *J. Phys. Chem. Lett.*, **4**, No. 9: 1570 (2013).
48. https://genesisnanotech.wordpress.com/2014/12/19/dye-sensitized-solar-cells-and-new-solar-energy-material-perovskite-19-conversion-efficiancy.
49. M. Nazeeruddin, A. Ray, I. Rodicio, R. Humphry-Baker, E. Mueller, P. Liska, N. Vlachopoulos, and M. Graetzel, *J. Am. Chem. Soc.*, **115**, No. 14: 6382 (1993).
50. M. Nazeeruddin, P. Pechy, T. Renouard, S. M. Zakeeruddin, R. Humphry-Baker, P. Comte, P. Liska, L. Cevey, E. Costa, V. Shklover, L. Spiccia, G.B. Deacon, C.A. Bignozzi, and M. Gratzel, *J. Am. Chem. Soc.*, **123**, No. 8: 1613 (2001).
51. K.F. Chou and A.M. Dennis, *Sensors,* **15**, No. 6: 13288 (2015).
52. Z. Abdin, M.A. Alim, R. Saidur, M.R. Islam, W. Rashmi, S. Mekhilef, and A. Wadi, *Renew. Sust. Energy Rev.*, **26**: 837 (2013).
53. Y. Bai, I. Mora-Sero, F. De Angelis, and P. Wang, *Chem. Rev.*, **114**, No. 19: 10095 (2014).
54. J. Llorca, *Contrib. Sci.*, **7**, No. 1: 57 (2011).
55. https://esdr.lbl.gov/news/article/11190/berkeley-lab-research-helps-fuel-cells-meet-their-potential.
56. DOE Technical Targets for Onboard Hydrogen Storage for Light-Duty Vehicles; https://www.energy.gov/eere/fuelcells/doe-technical-targets-onboard-hydrogen-storage-light-duty-vehicles.
57. A. Zuttel, P. Sudan, Ph. Mauron, T. Kiyobayashi, Ch. Emmenegger, and L. Schlapbach, *Int. J. Hydrogen Energy*, **27**, No. 2: 203 (2002).

58. I.P. Jain, P. Jain, and A. Jain, *J. Alloys Compd.*, **503**, No. 2: 303 (2010).
59. http://spie.org/newsroom/1451-designing-novel-carbon-nanostructures-for-hydrogen-storage?SSO=1.
60. I.Yu. Sagalyanov, Yu.I. Prylutskyy, T.M. Radchenko, and V.A. Tatarenko, *Usp. Fiz. Met.*, **11**, No. 1: 95 (2010) (in Ukrainian).
61. L.L. Kondratenko, O.V. Mykhailenko, Yu.I. Prylutskyy, T.M. Radchenko, and V.A. Tatarenko, *Usp. Fiz. Met.*, **11**, No. 3: 369 (2010) (in Ukrainian).
62. T.M. Radchenko, V.A. Tatarenko, I.Yu. Sagalianov, and Yu.I. Prylutskyy, *Graphene: Mechanical Properties, Potential Applications and Electrochemical Performance* (Ed. B.T. Edwards) (Hauppauge, N.Y., USA: Nova Science Publishers, Inc.: 2014), Ch. 7, p. 219.
63. A.C. Dillon, K.M. Jones, T.A. Bekkedahl, C.H. Kiang, D.S. Bethune, and M.J. Heben, *Nature*, **386**: 377 (1997).
64. P. Benard, R. Chahine, P. Chandonia, D. Cossement, G. Dorval-Douville, L. Lafia, P. Lachance, R. Paggiaro, and E. Poirier, *J. Alloys Compd.*, **446–447**: 380 (2007).
65. S. Beyaz, F. Darkrim Lamari, B. Weinberger, and P. Langlois, *Int. J. Hydrogen Energy*, **35**, No. 1: 217: (2010).
66. F. Darkrim, J. Vermesse, and P. Malbrunot, *J. Chem. Phys.*, **110**, No. 8: 4020 (1999).
67. Q. Wang and J.K. Johnson. *J. Chem. Phys.*, **110**, No. 1: 577 (1999).
68. M. Hirscher, M. Becher, M. Halushka, F. von Zeppellin, X. Chen, U. Dettlaff-Weglikowska, and S. Roth, *J. Alloys Compd.*, **356–357**: 433 (2003).
69. A.D. Lueking and R.T. Yang, *Appl. Catal. A*, **265**: 259 (2004).
70. G. Yushin, R. Dash, J. Jagiello, and Y. Gogotsi, *Adv. Funct. Mat.*, **16**, No. 17: 2288 (2006).
71. R. J.-M. Pelleng, F. Marinelly, J.D. Fuhr, F. Fernandez-Alonso, and K. Refson, *J. Chem. Phys.*, **129**, No. 22: 224701 (2008).
72. V. Bhat, C. Contescu, N. Gallego, and F. Baker, *Carbon*, **48**, No. 5: 1331 (2010).
73. J.L.C. Rowsell and O.M. Yaghi, *Angew. Chem. Int. Ed.*, **44**, No. 30: 4670 (2005).
74. N.L. Rosi, J. Eckert, M. Eddaoudi, D.T. Vodak, J. Kim, M. O'Keeffe, and O.M. Yaghi, *Science*, **300**, No. 5622: 1127 (2003).
75. G. Ferey, M. Latroche, C. Serre, F. Millange, T. Loiseau, A. Percheron-Guegan, *Chem. Commun.*, **0**, No. 24: 2976 (2003).
76. M. Hirscher, B. Panella, and B. Schmitz, *Micropor. Mesopor. Mat.*, **129**, No. 3: 335 (2010).
77. D.J. Collins and H.C. Zhou, *J. Mat. Chem.*, **17**, No. 30: 3154 (2007).
78. M. Latroche, S. Surble, C. Serre, C. Mellot-Draznieks, P.L. Llewellyn, J.H. Lee, J.S. Chang, S.H. Jhung, and G. Ferey, *Angew. Chem. Int. Ed.*, **45**, No. 48: 8227 (2006).
79. A.G. Wong-Foy, A.J. Matzger, and O.M. Yaghi, *J. Am. Chem. Soc.*, **128**, No. 11: 3494 (2006).
80. H.K. Chae, D.Y. Siberio-Perez, J. Kim, Y.B. Go, M. Eddaoudi, A.J. Matzger, M. O'Keeffe, and O.M. Yaghi, *Nature*, **427**: 523 (2004).
81. J.L.C. Rowsell and O.M. Yaghi, *Angew. Chem. Int. Ed.*, **44**, No. 30: 4670 (2005).
82. J.L.C. Rowsell, A.R. Millward, K.S. Park, and O.M. Yaghi, *J. Amer. Chem. Soc.*, **126**, No. 18: 5666 (2004).
83. G. Sandrock, *J. Alloys Compd.*, **293–295**: 877 (1999).
84. R. Wiswall, *Hydrogen in Metals II. Application-Oriented Properties* (Eds. G. Alefeld and J. Völkl) (Berlin–Heidelberg: Springer-Verlag: 1978), Ch. 5, p. 201.

85. Y. Fukai, *The Metal–Hydrogen Systems. Basic Bulk Properties* (Berlin–Heidelberg: Springer-Verlag: 2005).
86. A. Zaluska, L. Zaluski, and J.O. Ström-Olsen, *J. Alloys Compd.*, **288**, Nos. 1–2: 217 (1999).
87. G. Barkhordarian, T. Klassen, and R. Bormann, *J. Alloys Compd.*, **364**, Nos. 1–2: 242 (2004).
88. M.U. Niemann, S.S. Srinivasan, A.R. Phani, A. Kumar, D.Y. Goswami, and E.K. Stefanakos, *J. Nanomaterials*, **2008**: 950967 (2008).
89. G. Liang, J. Huot, S. Boily, and A. Van Neste, *J. Alloys Compd.*, **292**, Nos. 1–2: 247 (1999).
90. F. Gennari, F. Castra, G. Urretavizcaya, and G. Meyer, *J. Alloys Compd.*, **334**, Nos. 1–2: 277 (2002).
91. W. Oelerich, T. Klassen, and R. Bormann, *J. Alloys Compd.*, **322**, Nos. 1–2: L5 (2001).
92. G. Liang, J. Huot, S. Boily A. Van Neste, and R. Schulz, *J. Alloys Compd.*, **291**, Nos. 1–2: 295 (1999).
93. H.G. Schimmel, J. Huot, L.C. Chapon, F.D. Tichelaar, and F.M. Mulder, *J. Am. Chem. Soc.*, **127**, No. 41: 14348 (2005).
94. Z. Dehouche, R. Djaozangry, J. Huot, S. Boily, J. Goyette, T. K. Bose, and R. Schulz, *J. Alloys Compd.*, **305**, Nos. 1–2: 264 (2000).
95. K.S. Jung, E.Y. Lee, and K.S. Lee, *J. Alloys Compd.*, **421**, Nos. 1–2: 179 (2006).
96. W. Oelerich, T. Klassen, and R. Bormann, *J. Alloys Compd.*, **315**, Nos. 1–2: 237 (2001).
97. K. Higuchi, Y. Yamamoto, H. Kajioka, K. Toiyama, M. Honda, and S. Orimo, *J. Alloys Compd.*, **330–332**: 526 (2002).
98. K. Higuchi, H. Kajioka, K. Toiyama, H. Fujii, S. Orimo, and Y. Kikuchi, *J. Alloys Compd.*, **293–295**: 484 (1999).
99. H. Akyildiz, M. Ozenbas, and T. Ozturk, *Int. J. Hydrogen Energy*, **31**, No. 10: 1379 (2006).
100. T. Richardson, B. Farangis, J. Slack, P. Nachimuthu, R. Perera, N. Tamura, and M. Rubin, *J. Alloys Compd.*, **356–357**: 204 (2003).
101. P. Chen, Z. Xiong, J. Luo, J. Lin, and K. L. Tan, *Nature*, **420**: 302 (2002).
102. H. Leng, T. Ichikawa, S. Isobe, S. Hino, N. Hanada, and H. Fujii, *J. Alloys Compd.*, **404–406**: 443 (2005).
103. T. Ichikawa, S. Isobe, N. Hanad, and H. Fujii, *J. Alloys Compd.*, **365**, Nos. 1–2: 271 (2004).
104. Z. Xiong, J. Hu, G. Wu, P. Chen, W. Luo, K. Gross, and J. Wang, *J. Alloys Compd.*, **398**, Nos. 1–2: 235 (2005).
105. Z. Xiong, G. Wu, J. Hu, and P. Chen, *J. Alloys Compd.*, **441**, Nos. 1–2: 152 (2007).
106. W. Luo, *J. Alloys Compd.*, **381**, Nos. 1–2: 284 (2004).
107. J. Yang, A. Sudik, D. Siegel, D. Halliday, A. Drews, R. O. Carter, C. Wolwerton, G.J. Lewis, J.W.A. Sachtler, J.J. Low, S.A. Faheem, D.A. Lesch, and V. Ozolins, *Angew. Chem. Int. Ed.*, **47**, No. 5: 882 (2008).
108. A. Goncharov, A. Guglya, and E. Melnikova, *Int. J. Hydrogen Energy*, **37**, No. 23: 18061 (2012).
109. A. Goncharov, A. Guglya, A. Kalchenko, E. Solopikhina, V. Vlasov, and E. Lyubchenko, *J. Nanotechnology*, **2017**: 4106067 (2017).
110. K. Papathanassopoulos and H. Wenzl, *J. Phys. F: Metal Phys.*, **12**, No. 7: 1369 (1982).

111. H. Numakura and M. Koiwa, *Acta Metall.*, **32**, No. 10: 1799 (1984).
112. S.R. Peddada, I.M. Robertson, and H.K. Birnbaum, *Mater. Res.*, **8**, No. 2: 291 (1993).
113. A. Guglya, E. Lyubchenko, Yu. Marchenko, E. Solopikhina, and V. Vlasov, *Int. J. Hydrogen Energy*, **41**, No. 22: 9410 (2016).
114. A. Fujishima, K. Kohayakawa, and K. Honda, *J. Electrochem. Soc.*, **122**, No. 11: 1487 (1975).
115. E. Nyankson, B. Agyei-Tuffour, J. Asare, E. Annan, E.R. Rwenyagila, D. Konadu, A. Yaya, and D.D. Arhin, *J. Engineer. Appl. Sci.*, **8**, No. 10: 871 (2013).
116. http://statnano.com/news/45676.
117. https://www.forbes.com/sites/peterdiamandis/2014/09/02/solar-energy-revolution-a-massive-opportunity/#1ba9e79a6c90.
118. https://www.canadiansolar.com/making-the-difference/surprises-in-solar.html.
119. E. Serrano, G. Rus, and J. Garcia-Martinez, *Renew. Sust. Energy Rev.*, **13**, No. 9: 2373 (2009).
120. *Renewables 2017 Global Status Report* (Paris: REN21: 2017); http://www.ren21.net/wp-content/uploads/2017/06/17-8399_GSR_2017_Full_Report_0621_Opt.pdf.
121. A. Konechenkov, *Terminal*, No. 26 (820): 12 (2016); http://uwea.com.ua/uploads/publications/TERMINAL_27.06.2016.pdf (in Russian).
122. V. Sidorovich, *Ehlektricheskaya Generatsiya v Germanii: Osnovnye Itogi 2016* [Power Generation in Germany — Assessment of 2016]; http://renen.ru/elektroenergetika-germanii-osnovnye-itogi-2016 (in Russian).

Received August 3, 2018;
in final version, October 25, 2018

О.Г. Гугля[1], *В.А. Гусєв*[2], *О.А. Любченко*[3]

[1] Національний науковий центр «Харківський фізико-технічний інститут» НАН України, вул. Академічна, 1; 61108 Харків, Україна
[2] Північно-Східний науковий центр НАН і МОН України, вул. Багалія, 8; 61000 Харків, Україна
[3] Національний технічний університет «Харківський політехнічний інститут», вул. Кирпичова, 2; 61002 Харків, Україна

ВІД НАНОМАТЕРІЯЛІВ І НАНОТЕХНОЛОГІЙ ДО АЛЬТЕРНАТИВНОЇ ЕНЕРГЕТИКИ

Питання використання альтернативних джерел енергії в різних областях промисловости та в побуті набуває все більшої актуальности. Це зумовлено тим, що виснажуються джерела вуглеводневої сировини й, одночасно з цим, використання вуглеводнів призводить до погіршення екологічної обстановки та забруднення навколишнього середовища. Серед різних можливих джерел відновлюваної енергії сонячна та воднева енергії вважаються найбільш перспективними. Головною перешкодою на шляху їх широкого використання та поширення вважається відсутність матеріялів, які можуть ефективно перетворювати енергію Сонця та водню в електрику й тепло. Основними вимогами до таких матеріялів є висока енергетична місткість, структурна стабільність і низька ціна. Ці властивості притаманні нанокристалічним матеріялам; тому саме їм присвячено численні дослідження останніх десятиліть. У даному огляді особлива увага приділяється

трьом видам нанокристалічних об'єктів, що представляють найбільший інтерес для енергетики, а саме, сонячним елементам, літій-йонним батареям і твердотільним накопичувачам водню. Розглянуто їхні структурні особливості, технології виготовлення, а також взаємозв'язок між структурою й енергетичною місткістю. Проаналізовано стан і перспективи використання нанокристалічних структур у відновлюваній енергетиці.

Ключові слова: альтернативна енергетика, наноматеріяли, сонячні елементи, літій-йонні батареї, накопичення водню.

А.Г. Гугля[1], *В.А. Гусев*[2], *Е.А. Любченко*[3]

[1] Национальный научный центр
«Харьковский физико-технический институт»,
ул. Академическая, 1; 61108 Харьков, Украина

[2] Северо-Восточный научный центр НАН и МОН Украины,
ул. Багалея, 8; 61000 Харьков, Украина

[3] Национальный технический университет
«Харьковский политехнический институт»,
ул. Кирпичёва, 2; 61002 Харьков, Украина

ОТ НАНОМАТЕРИАЛОВ И НАНОТЕХНОЛОГИЙ К АЛЬТЕРНАТИВНОЙ ЭНЕРГЕТИКЕ

Вопрос использования альтернативных источников энергии в различных областях промышленности и в быту приобретает всё большую актуальность. Это обусловлено тем, что истощаются источники углеводородного сырья и, одновременно с этим, использование углеводородов ведёт к ухудшению экологической обстановки и загрязнению окружающей среды. Среди различных возможных источников возобновляемой энергии солнечная и водородная энергии считаются наиболее перспективными. Главным препятствием на пути их широкого использования и распространения считается отсутствие материалов, которые могут эффективно превращать энергию Солнца и водорода в электричество и тепло. Основными требованиями к таким материалам являются высокая энергетическая ёмкость, стабильность и низкая цена. Этими качествами обладают нанокристаллические материалы; поэтому именно им посвящены многочисленные исследования последних десятилетий. В данном обзоре особое внимание уделяется трём видам нанокристаллических объектов, представляющих наибольший интерес для энергетики, а именно, солнечным элементам, литий-ионным батареям и твёрдотельным накопителям водорода. Рассмотрены их структурные особенности, технологии изготовления, а также взаимосвязь между структурой и энергетической ёмкостью. Проанализировано состояние и перспективы использования нанокристаллических структур в возобновляемой энергетике.

Ключевые слова: альтернативная энергетика, солнечные элементы, литий-ионные батареи, накопление водорода.